Greater than one billion optical Q factor for on-chip microresonators

Thesis by
LUE WU

In Partial Fulfillment of the Requirements for the
Degree of
Doctor of Philosophy

CALIFORNIA INSTITUTE OF TECHNOLOGY
Pasadena, California

2024
Defended September 11th, 2023

To my parents,
and my paternal grandparents,
and my maternal grandparents,
and my whole family,
and my girlfriend.

ACKNOWLEDGEMENTS

In those days, the smiths of Vahala surpassed all that they had contrived before; and they took thought, and they made Rings of Power, a.k.a. ultra-high-Q optical microresonators.

In my mind, the most exciting advances have always been enabled by optics. And there is every reason to believe that optics and photonics will continue to dramatically shape our world and make it a better place. I became involved in optics and photonics first and foremost because the discoveries and transformative technologies that it has enabled are extremely exciting to me beyond any words. Also, I have always dreamed of making my own contributions to this booming field.

I enjoyed and had a lot of fun in my 5-year graduate student journey (starting on July 9th, 2018). It was a special Ph.D. program, a unique period of time in Caltech history, even in human history. Two years of the COVID-19 pandemic started at the end of my G2 (March 2020) and extended to my G4 (Sept 2021). I didn't see my advisor in person for 18 months, while we were restricted from the lab and locked down at home. I deeply remember the times when everywhere was empty and I was always alone on campus. In the post COVID-19 era, big inflation followed, which I could strongly feel from price increases in food, rent, and gas. Big technological breakthroughs took place in these five years, including Artificial Intelligence (AI) and ChatGPT powered by Nvidia GPU and the popular appearances of electrical vehicles from Tesla.

I would like to express my sincere gratitude to my advisor, **Professor Kerry John Vahala**, for his encouragement and support throughout my graduate studies at Caltech. His keen devotion to science and diligent work ethic have deeply impacted me. He is super nice, encouraging, and supportive. I still remember when I was in my first year, I brought some "rubbish" results to him and I was very worried, his response was always positive "Great! Interesting! Keep going.", which helped me establish my confidence. I'm deeply grateful for the resources, energy, and time he invested in my education and training. He devoted considerable time to reviewing, editing, and polishing my manuscripts, significantly enhancing their quality. He is my role model for a professor. It has been a privilege to be a member of high highly motivated and talented group.

I would thank my committee members: Professor Andrei Faraon, Professor Oskar

Painter, and Professor Alireza Manradi, for serving in my committee. Special thanks to Andrei to serve as my committee chair. Oskar's quantum optics lectures (APh190C) were very very interesting and fun to learn those beautiful knowledge. Alireza and his group helped me a lot in research and we had many insightful talks.

I would thank all the professors in Caltech who instructed me and presented lectures during the many courses I took.

I would thank my parents, my paternal grandmother, and all my family members. They supported me during my whole adventure and video call with me every week (Saturday evening). I saw my mother in Sept 2019 and it was my only time for me to see my family in person for thees last 5 years. Unfortunately, my maternal grandmother passed away in March 2019, which is my biggest fear when I am abroad, and I really miss her.

My heartful gratitude belongs to my girlfriend Haoyu Li (Yoyo). She took care of my life throughout my time in graduate school and cooked more than one thousand meals for us. She is my best counsel for the many decisions I've made. She also assisted me in making paper figures and polishing presentations. She traveled with me to many places across America. She played video games (such as Assassin's Creed Valhalla) using my PS5 and Nintendo Switch and watched movies with me.

I would offer sincere thanks to my fellow labmates in Vahala group, some of whom were my mentors in many aspects, for all the fruitful discussions between us. They are Prof. Qifan Yang, Dr. Myoung-Gyun Suh, Prof. Chengying Bao, Dr. Yu-Hung Lai, Dr. Boqiang Shen, Dr. Heming Wang, Zhiquan Yuan, Yukun Lu, Maodong Gao, Qing-Xin Ji (Andrew), Bohan Li, Anna Shelton, Yan Yu, Peng Liu, Kellan Colburn, Dr. Hao-Jing Chen, Jinhao Ge, and Jin-Yu Liu. I'd also like to extend my gratitude to our group's alumni for the countless enjoyable meals, conversations, and meetings we've shared. They include but are not limited to Prof. Kiyoul Yang, Prof. Xu Yi, Prof. Hansuek Lee, Dr. SeungHoon Lee, Dr. Jiang Li, and Dr. Dongyoon Oh (James). Specifically, I would thank the group associate Dr. Henry A. Blauvelt (Hank) for fruitful discussions and his wise advice on my career. Last but not least, I would thank the administrative assistants Cecilia A. Gamboa, Connie M. Rodriguez, Jennifer Blankenship, and Christy Jenstad and the other grant managers. In particular, I understand how much work Cecilia needs to handle every day, which is incredible to me.

Special thanks are also offered to my research intern advisor at Harvard University,

Professor Marko Loncar, as well as my mentors Prof. Linbo Shao, Prof. Cheng Wang, and the other lab mates. I was super fortunate to enter integrated photonics field as a member of Loncar group.

I would also thank my research collaborators, who cover a broad spectrum. They include but are not limited to **Professor John Edward Bowers**, Dr. Warren Jin, Prof. Chao Xiang, Jeol Guo, Prof. Lin Chang, Prof. Weiqiang Xie, Theodore J. Morin, Dr. Mingxiao Li, and David Kinghorn at UCSB; Dr. Andrey B. Matsko, Dr. Vladimir S Ilchenko, and Dr. Wei Zhang at JPL; Prof. Scott Diddams at NIST; Prof. Amnon Yariv at Caltech; Prof. Harry A. Atwater and Prof. Wen-Hui Cheng (Sophia) at Caltech; Dr. Myoung-Gyun Suh, Dr. Yonghwi Kim, Mostafa Honari, Dr. Byoung Jun Park, and Dr. Sudip Gurung at NTT Research; Prof. Qiang Lin, Dr. Yang He, and Dr. Jingwei Ling at Rochester: Dr. Weimin Zhou, Dr James P. Cahill, and Dr. Tanvir Mahmood at ARL and Prof. Curtis R Menyuk at UMBC; Dr. James Gates, Dr. Christopher Holmes, and Dr. Bruno Moog at University of Southampton; Stephan Amann and Dr. Nathalie Picque at MPQ; Dr. Cort Johnson at Draper Lab; Dr. Mario Paniccia and Avi Feshali at Anello Photonics; DARPA DODOS team collaboration under Prof. John Bowers as PI; DARPA LUMOS team collaboration under my advisor as PI; and DARPA GRYPHON team collaboration under my advisor as PI.

I gratefully acknowledge the critical support and infrastructure provided by Kavli Nanoscience Institute (KNI) at Caltech, Nanofabrication Facility (NanoFab) at UCSB, NanoLab at UCLA, Caltech Microanalysis Center (CMC) and Dr. Yunbin Guan in Caltech Division of Geological and Planetary Sciences, as well as Biological Imaging Facility (BIF), Dr Giada Spigolon, and Molecular Materials Resource Center (MMRC) at Caltech Beckman Institute.

I gratefully acknowledge the funding agencies to support Vahala group research and my reserach activities. They include but not limited to DRAPA, DTRA, ARL, and NTT Research.

I would thank my friends at Caltech. Especially, I would sincerely thank Ruide Fu (Frid) and Yuqi Zhang for their sweet accompaniment during the pandemic and the beautiful classical music we enjoyed together. Also, I would sincerely thank Robert M. Gray (Robby) for his encouragement and help in winter 2021. I would thank Zexuan Niu for his invitation to visit Iowa, a beautiful state. I would thank Prof. Jin Yang and Dr. Lu Xu for their help and guidance during my early years. I would thank Danyang Cai for her encouragement. I would thank Jiabao Ren for her inspiration. Also, I would thank my Caltech roommates: Tianzhe Zheng (Terry), Tian Xie, Benjamin Kuang-Yuan Chang, and Yifan Chen. I would thank Duxing Hao (Jason) and Xuejian Shen (Jacob) for travelling together with me to many national parks. I'd like to extend my thanks to Yicheng Bao at Harvard for the enjoyable anime-watching sessions we shared, and to Dr. Linghang Kong at MIT for the memorable movie nights we spent together.

I gratefully acknowledge all the support from Caltech. In particular, I would sincerely thank Dr. Lee H. Coleman, Dr. Mariel Tourani, and Dr. John Tsai for their taking good care of my health. Also, I would sincerely thank the Caltech housing, dining, cleaning, Student Wellness Services for Health and Counseling, shipping, facility, and security staff. I was fortunate enough to live in Cats (Caltech Student Housing) for more than 5 years.

I developed many hobbies and attended many interest groups during my time at Caltech, especially sports. I would thank the basketball pickup players every Wednesday and Friday evening, Caltech ballroom team, soccer teams I played in (Exfits and RLC United), water polo games, flag football games, and soccer pickups.

I really want to thank Xuening Cui (Cathy), an extraordinary lady with strong self-motivation and hardworking spirit, who encouraged, inspired, and firmly supported me during the time before Caltech and the first year in Caltech, especially in the process of application to graduate school. She is my role model and her characteristics deeply shaped me. This dissertation would be impossible without her.

I would also like to express my gratitude to Jinfang Shi for her support and inspiration during my college years, and for her infectious enthusiasm for technology.

Overall, my five years pursuing a PhD at Caltech have been one of the happiest times in my life. I am profoundly grateful for everything.

Figure 0.1: Wedge-resonator-like structure on Caltech campus.

ABSTRACT

This thesis is focused on making ultra-high-Q optical microresonators on silicon chips based on design and constructing ultra-low-loss optical waveguides (with losses around 20 dB/km), their fabrication process development, and device applications in on-chip nonlinear optics, including frequency combs, low-noise microwave generation, and narrow-linewidth lasers.

First, using thermally grown oxide (thermal silica) and wedge microresonator structure, a record Q factor exceeding 1.1 billion is achieved. Then, the limitations of the Q-factor due to surface roughness scattering loss and OH absorption loss are investigated and identified. Absorption limited Q-factor of 8 billion mainly attributed to OH ions is measured. To further explore the potential of thick thermal silica as under cladding material, wedge resonator fabricated in 25-μm-thick thermal silica achieves a Q-factor of over 60 million, along with a sixfold improvement in thermal stability and a 5 billion absorption-limited Q-factor. Subsequently, low noise microwave signal generation is demonstrated using these devices in a fully optical packaged form, operating soliton microcomb to generate beatnote microwave signals. Noise limitations arising from dispersive waves induced by distinct transverse modes are identified. Additionally, a low-fundamental-linewidth microcavity Brillouin laser is demonstrated, benefiting from device high Q-factor. The noise limits stemming from thermal refractive fluctuation at low offset frequencies and laser output power at high offset frequencies are identified. To improve device integration level, an engineered reduction of interface scattering using TM mode enables a demonstration of 700 million Q factor in a fully-integrated high-aspect-ratio thin SiN platform fabricated in a CMOS foundry. To add one more thing, room temperature soliton microcomb generation is demonstrated for the first time in high-Q AlGaAs microresonators.

PUBLISHED CONTENT AND CONTRIBUTIONS

1. Wu, L., Gao, M., Liu, J.-Y., Chen, H.-J., Colburn, K., Blauvelt, H. A. & Vahala, K. J. "Hydroxyl ion absorption in on-chip high-Q resonators". *Opt. Lett.* **48,** 3511–3514. `http://dx.doi.org/10.1364/OL.492067` (2023).
   L.W. led the project, designed and fabricated the devices, measured the data, ran simulations and data analysis, wrote manuscripts with the assistance from all the other authors.

2. Wu*, L., Xie*, W., Chen*, H.-J., Colburn, K., Xiang, C., Chang, L., Jin, W., Liu, J.-Y., Yu, Y., Yamamoto, Y., Bowers, J. E., Suh, M.-G. & Vahala, K. J. "AlGaAs soliton microcombs at room temperature". *Opt. Lett.* **48,** 3853–3856. `http://dx.doi.org/10.1364/OL.484552` (2023).
   L.W. led the project, conceived the idea, measured the data, ran simulations and data analysis, wrote manuscripts with the assistance from all the other authors.

3. Wang*, H., Wu*, L., Yuan*, Z. & Vahala, K. "Towards milli-Hertz laser frequency noise on a chip". in *CLEO* (2021), SF2O.2. `http://dx.doi.org/10.1364/CLEO_SI.2021.SF2O.2`.
   L.W. designed and fabricated the devices, collabrated with the other leading authors to conduct measurements, run simulations, conduct data analysis and prepare the manuscript.

4. Yang*, Q.-F., Ji*, Q.-X., Wu*, L., Shen, B., Wang, H., Bao, C., Yuan, Z. & Vahala, K. "Dispersive-wave induced noise limits in miniature soliton microwave sources". *Nature Communications* **12,** 1442. `https://doi.org/10.1038/s41467-021-21658-7` (2021).
   L.W. designed and fabricated the devices, packaged the devices into functional modules, participated in module operation, soliton generation, measurements, data analysis, and paper writing.

5. Wu, L., Wang*, H., Yang, Q.-F., Ji, Q.-X., Shen, B., Bao, C., Gao, M. & Vahala, K. "Greater than one billion Q factor for on-chip microresonators". *Opt. Lett.* **45,** 5129–5131. `http://dx.doi.org/10.1364/OL.394940` (2020).
   L.W. led the project, designed and fabricated the devices, measured the data, ran simulations and data analysis, wrote manuscripts with the assistance from all the other authors.

$*$ These authors contributed equally to this work.

TABLE OF CONTENTS

LIST OF ILLUSTRATIONS

LIST OF TABLES

NOMENCLATURE

κ $\kappa_{\mathbf{L}}$ $\kappa_{\mathbf{tot}}$**.** Total loss rate.

κ_0 $\kappa_{\mathbf{i}}$**.** Intrinsic loss rate.

κ_1 $\kappa_{\mathbf{ex}}$ $\kappa_{\mathbf{c}}$**.** Coupling rate.

Q $Q_{\mathbf{L}}$ $Q_{\mathbf{tot}}$**.** Loaded/total Q-factor.

Q_0 $Q_{\mathbf{i}}$**.** Intrinsic Q-factor.

Q_1 $Q_{\mathbf{ex}}$ $Q_{\mathbf{C}}$**.** Coupling/external Q-factor.

CMOS. Complementary metal–oxide–semiconductor.

FSR. free-spectral-range.

thermal oxide. Thermally grown silica layer on silicon wafers.

Chapter 1

INTRODUCTION

1.1 Historical perspective

Light is present in everybody's everyday life. To engineer, control, amplify and purify light as a tool to serve mankind is an eternal pursuit.

Since the invention of the laser enabled by optical cavity [1, 2], optics and photonics have revolutionized science and technology. The Internet would be impossible without the ultra-high-bandwidth ultra-low-loss information transmission made possible by fiber optic communications. For scientific explorations, gravity waves were detected using amazing laser interferometers (LIGO). Also, special mode locked lasers called frequency combs [3] now make possible the most accurate clocks in the world. And exotic states of matter are only possible through the process of laser cooling. Indeed, optical physics and photonics have become key technological and scientific pillars on which the modern world rests.

Low optical loss is one of the major considerations to design an optical and photonic device/system. Low loss enables efficient transportation of energy and information through light. One example is the fiber communication enabled by ultra-low loss, which deeply shaped the modern world [4, 5]. For mass deployment of optical networks (such as in data centers), low loss means low power dissipation, small heat generation, high energy efficiency, and high signal fidelity. Low loss also enables enormous multiplication of light electric field intensity using a structure called optical cavity to enhance light-matter interactions, which enabled lasers.

Dielectric optical waveguide technology provides an effective solution to control light propagation, boasting several essential properties. Dielectric materials offer a diverse selection pool with a wide range of properties, affording considerable design flexibility. An engineered difference in refractive index between the core and cladding conveniently confines light to an area measured in μm^2, thereby avoiding free-space diffraction. The waveguides can be designed to bend, enabling the light to be directed in any desired direction. Moreover, these devices can be fabricated on semiconductor wafers like silicon wafers using well-established semiconductor fabrication technology, particularly electronic CMOS technology. Such flexibility in bending allows for the high-density deployment of devices, paving the way for interconnected system construction known as integrated photonics.

The arbitrarily light bending property of dielectric optical waveguides allows for the construction of specialized structures, such as making a waveguide into a loop. This operation creates a special type of devices: optical cavity, or called optical resonator. The optical resonance conditions are based on the facts that light is a wave and can coherently interference to add up together when each round-trip of propagating light are **in phase**. Compared with Fabry–Perot cavities, where the mirrors can only reverse the direction of light, such cavities offer greater design flexibility.

The combined concepts of integrated photonics and optical cavity have led to the development of an important class of devices: **optical microcavity**, also known as **optical microresonator** [6] in the on-chip form.

The applications of optical microcavities can be categorized into the following main classes:

1. Enhance light intensity to enable access to **nonlinear optics**, which offers superior performance in terms of **coherence**, such as frequency combs [7–9], narrow-linewidth lasers [10], low-noise microwave generations, mode locking to form pulses [11].
2. In frequency domain, provide a narrow stable spectral feature, so that laser can reference to it using techniques such as Pound-Drever-Hall (PDH) [12] or feedback to semiconductor laser (SL's) to narrow its linewidth using techniques such as injection locking [13].
3. Study light-matter interactions such as in cavity quantum electrodynamics (cavity QED), cavity optomechanics [14, 15].
4. Enhance electro-optical (EO) modulation efficiency such as in Si microring EO modulators [16] for transmitters and inter-chip data communications.
5. On system level, construct miniature precision metrology systems [17, 18].
6. Spectral filter.
7. Reflector.

High optical Q factor is critically important in optical microcavities where it determines performance for almost all these applications.

Q factor frequently enters quadratically into device performance. For example, in Raman [19], parametric [20, 21], and Brillouin [22–24] nonlinear optical oscillators, threshold varies inverse quadratically with Q. Moreover, this same Q dependence enters the fundamental linewidth of laser oscillators [2] such as microcavity Brillouin lasers [10] and self injection locked semiconductor lasers [25]. Ultimately, these considerations are key performance drivers in soliton microcomb systems [11], microresonator gyroscopes [26–29], and microwave sources [30, 31]. At the same time, the many benefits of high Q factors have stimulated remarkable progress in boosting its value across a range of material systems and device platforms, spanning both on-chip platforms — such as thermal silica [24, 32, 33], fused silica [34], high index silica [35], high aspect ratio thin silicon nitride (SiN around 100 nm) [13, 36, 37], thick SiN (around 800 nm) [38, 39], Si (Si on insulator, SOI) [40], thin film lithium niobate (TFLN) [41], AlGaAs [42, 43], tantala [44], aluminum nitride (AlN) [45], gallium phosphide [46], diamond [47], silicon carbide (SiC) [48], chalcogenide [49], SiGe [50] — as well as other forms mainly in whispering gallery mode (WGM) such as fiber tip microsphere [51], crystalline (MgF_2 and CaF_2) [52], fiber preform [53], lithium niobate, lithium tantalate, and sapphire [54].

In addition to optical quality factors (Q), various other properties of optical microresonator systems merit consideration during device design. These attributes encompass mode volume, mode area, dispersion, single mode operation, backscattering strength, robustness, quietness, nonlinearity strength (such as $\chi^{(2)}$, $\chi^{(3)}$), fabrication difficulty and compatibility, thermal properties, reliability, tuning capabilities. As is often the case, these requirements are to a certain extent mutually exclusive. A trade-off decision needs to be made when design a device.

Generally, the strategy aimed at improving the quality factor (Q) tend to be winning. For instance, enlarging the mode area and mode volume typically leads to an increase in Q, and Q is approximately proportional to the mode volume (V). Given that the threshold for parametric oscillation scales as V/Q^2, opting for a larger mode area in exchange for a greater Q results in a Q^2 advantage

Thermal silica has a unique place in the high-Q world both because its losses are extremely low and also it has many favorable qualities for low noise operation of combs, lasers and other devices compared to other material platforms. For example, the low n_2 and the ability to operate with large mode volumes are both advantageous.

A logical goal is to push the Q-factor as high as possible while making some trade-offs and along this investigation, understand the device physics which sets the limits so that device performance can be optimized for a particular application. By doing this one might be find ways to modify either material or structure to make devices which are well performing for certain applications. To explain further and to provide an introduction to the basic concepts and topics covered in this thesis, we now review optical microresonators and thermal silica wedge microresonators.

A basic familiarity with this topic is assumed throughout this thesis. For more comprehensive reviews of optical microresonators, the reader is referred to references such as Vahala [6].

1.2 Optical microresonator

In optical resonators (cavities), Q-factor (quality factor) is a dimensionless measure of the optical storage time of light in the resonator. High-Q means that light coupled into the resonator is stored for longer periods of time.

$$Q = \omega\tau = \frac{\omega}{\kappa} \tag{1.1}$$

Q factor is inversely proportional to the optical loss in the constituent waveguides.

$$Q_0 = 4343 \times \frac{2\pi n_g}{\lambda\alpha} \tag{1.2}$$

where Q_0 is intrinsic Q-factor (billion), n_g is the group refractive index, λ is the wavelength (nm), and α is the optical propagating loss (dB/km).

$$Q^{-1} = Q_0^{-1} + Q_\mathrm{C}^{-1} \tag{1.3}$$

Indeed, the various attributes of optical microresonators are intrinsically linked to the properties of their constituent waveguides.

Microresonator free-spectral-range (FSR) is determined by waveguide group index (n_g) (group velocity (v_g)):

$$\mathrm{FSR}_\mathrm{Hz} = \frac{v_\mathrm{g}}{L} = \frac{c}{n_\mathrm{g} \cdot L} \tag{1.4}$$

where L is microresonator single round-trip length.

Microresonator second-order dispersion parameter (D_2) is determined by waveguide group velocity dispersion (GVD) (β_2):

$$D_2 = -\frac{c}{n_\mathrm{g}} D_1^2 \cdot \beta_2 \tag{1.5}$$

where $D_1 = 2\pi \times \text{FSR}$.

As a natural consequence, microresonators serve as a powerful tool for assessing various optical waveguide properties, including loss, group velocity, and group velocity dispersion (GVD). They are also highly effective for characterizing material properties such as absorption rates [55] and impurity concentrations [56].

The microresonator critical coupling condition is reached when the intrinsic loss rate κ_i equals coupling rate κ_{ex} [57]:

$$\kappa_i = \kappa_{\text{ex}} \tag{1.6}$$

Equivalently,

$$Q_0 = Q_{\text{C}} \tag{1.7}$$

This condition for coupling indicates that a higher quality factor (Q) not only eases the coupling requirements but also brings additional advantages. Specifically, when the intrinsic loss κ_i is minimized, the associated required coupling loss κ_{ex} is reduced. This reduction allows for a greater separation between the coupling waveguide and the microresonator. In turn, perturbations from the coupling waveguide to the microresonator—which is usually perfectly symmetric—are diminished, as is perturbation-induced scattering loss, a component of the intrinsic loss. Consequently, the intrinsic loss κ_i is further reduced, leading to even higher quality factor (Q).

The microresonators enhance the circulating intensities by a factor, defined by the ratio of Q factor and cavity mode volume (V)

$$I_{\text{circ}} = P_{\text{in}} \frac{\lambda}{2\pi n_g} \frac{Q}{V} \tag{1.8}$$

$$I_{\text{circ}} = 3\ \text{GW/cm}^2 \tag{1.9}$$

$$P_{\text{in}} = 1\ \text{mW} \tag{1.10}$$

$$P_{\text{circ}} = \frac{1}{2\pi} P_{\text{in}} \mathcal{F} \tag{1.11}$$

Because the resonators themselves are very small in both cross section (effective mode area A_{eff}) and diameter dimensions, the resulting stored optical energy is confined to an extraordinarily small mode volume (effective mode volume V_{eff}). This, in turn, results in very large circulating intensities (MegaWatt/cm^2) even with relatively low (about 1 milliWatt) input power levels. These intensities are high enough to access all of the nonlinear phenomena of the dielectric used to fabricate resonators.

When the nonlinear gain exceeds the loss, the oscillation starts. For instance, the threshold for Kerr parametric oscillation is [20, 58]:

$$P_{\text{th}} = \frac{\pi n_{\text{g}} \omega A_{\text{eff}}}{4\eta n_2} \frac{1}{D_1 Q^2} = \frac{\omega n_{\text{g}}^2}{8 c n_2 \eta} \frac{V_{\text{eff}}}{Q^2} \tag{1.12}$$

where $\eta = Q/Q_{\text{ex}}$ characterizes the waveguide to resonator loading.

The enhanced electro-optical interactions within microresonators have paved the way for their extensive high-volume use in commercial applications. For instance, they feature prominently in silicon photonics (SiPh) microring modulators [16, 59], which are key components of optical pluggable transceiver modules widely deployed in data center networks. Additionally, they are integral to co-packaged optics (CPO) transceiver solutions, designed for high-performance computing (HPC) systems [60].

1.3 Thermal silica wedge microresonator

Thermal oxidation is a CMOS (complementary metal–oxide–semiconductor) process. Thermal oxide is one of the most used material in CMOS systems. A unique property of silicon is that it can produce a very uniform oxide layer on the surface with little strain in the lattice, allowing the fabrication of from as thin as a few tens of angstroms (only a few atomic layers) such as gate-oxide layers to as thick as 25 microns such as under cladding layer for on-chip optical waveguides. In CMOS systems, in addition to serving as the gate dielectric, thermal oxide act as a protective coating in many steps of fabrication. Also, in areas between the devices, a thick layer of thermal oxide, called the "field oxide" (FOX) is grown, providing the foundation for interconnect lines that are formed in subsequent steps.

Thermal oxide is grown by placing the exposed silicon in an oxidizing atmosphere such as oxygen for dry oxidation and water for wet oxidation at a temperature around 1000°C.

The ultra-high-Q thermal silica wedge microresonator technology was first demonstrated in 2012 by Lee *et al.* [24] and the Q-factor as high as 875 million is achieved. The fabrication process steps are presented in Fig. 1.1. The optical modes are guided at the perimeter of the wedged silica disk. In 8 μm devices, mode area is around 60 μm^2. More details can be found in Chapter 2[33].

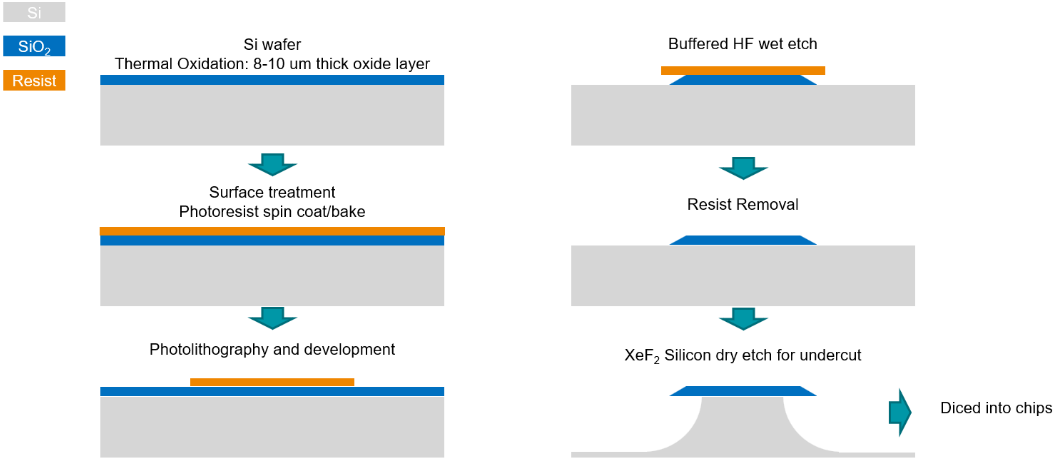

Figure 1.1: Fabrication process steps of thermal silica wedge microresonators.

The thermal silica wedge microresonators are usually probed using a fiber taper coupler [61–63]. By incorporating an additional process step, it is also feasible to create an integrated device featuring a silicon nitride (SiN) coupling waveguide [32].

As detailed in Suh *et al.* [64] (shown in Fig.1.2), an optical packaging technology has been developed to make thermal silica wedge microresonator chip a functional module.

Two key nonlinear optical effects are prominently featured in thermal silica wedge microresonators, leading to a multitude of important applications and demonstrations.

The dissipative Kerr soliton microcomb [11] formed in thermal silica wedge microresonators was first realized in 2015 by Yi *et al.* [58]. Building upon this groundbreaking comb technology, advancements have been made in various applications, including dual comb spectroscopy (DCS) [65, 66], dual comb ranging [67], and dual comb imaging [68].

The stimulated Brillouin laser (SBL) generated in thermal silica wedge microresonators was first successfully demonstrated in 2012 by Lee *et al.* [24] and Li *et al.*

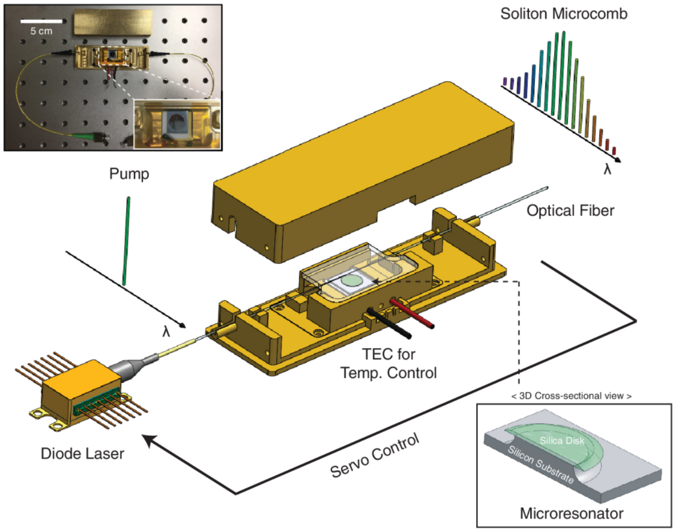

Figure 1.2: Schematics of a fiber-connectorized module with TEC temperature control. Upper left inset, a photograph of a 10 GHz soliton module with fiber pigtails. Lower right inset, a schematic cross-sectional view of a silica wedge disk resonator. Reprinted with permission from Suh *et al.* [64]

[10]. Leveraging this highly coherent light source, a range of powerful devices have been developed, including gyroscopes capable of measuring Earth's rotation [26, 29], as well as systems for electro-optical frequency division and stable microwave synthesis [69].

Chapter 2

GREATER THAN ONE BILLION Q-FACTOR ON CHIP: THERMAL SILICA WEDGE MICRORESONATORS

[1] Abstract

High optical quality (Q) factors are critically important in optical microcavities, where performance in applications spanning nonlinear optics to cavity quantum electrodynamics is determined. In this chapter, **a record Q factor of over 1.1 billion** is demonstrated for on-chip optical resonators. Using thermal silica whispering-gallery resonators on silicon, Q-factor data is measured over wavelengths spanning the C/L bands (100 nm) and for a range of resonator sizes and mode families. A record low sub-milliwatt parametric oscillation threshold is also measured in 9 GHz free-spectral-range devices. The results show the potential for thermal silica on silicon as a resonator material, establishing a new practical upper bound on Q using this CMOS compatible material.

The many applications of high optical quality (Q)-factor microresonators [6] have stimulated remarkable progress in boosting its value across a range of material systems and device platforms. Before this thesis work, for all the chip-based photonic systems, silica microresonators using thermally grown oxide (thermal silica) offered the highest Q factors, around 875 million [24]. In this chapter, by optimizing fabrication methods for thermal silica whispering-gallery resonators on silicon, the Q factor of this system has been boosted to **over 1.1 billion (a record on-chip Q-factor)**. The results are confirmed through linewidth, ring-down and parametric oscillation measurements.

In the investigation, wedge whispering-gallery resonator devices are fabricated using a combination of thermal oxidation (8 μm thickness on 4-inch high-purity float-zone silicon wafers), stepper projection optical lithography (i-line), buffered HF silica wet etch and XeF_2 silicon dry etch as detailed in reference [24]. The wedge angle was 27-30°. To boost overall Q performance, several process and mask layout improvements were implemented. The resist pattern and subsequent buffered HF

---

[1] Work presented in this chapter has been published in “Greater than one billion Q factor for on-chip microresonators," *Optics Letters* **45**, 5129-5131 (2020) [33]

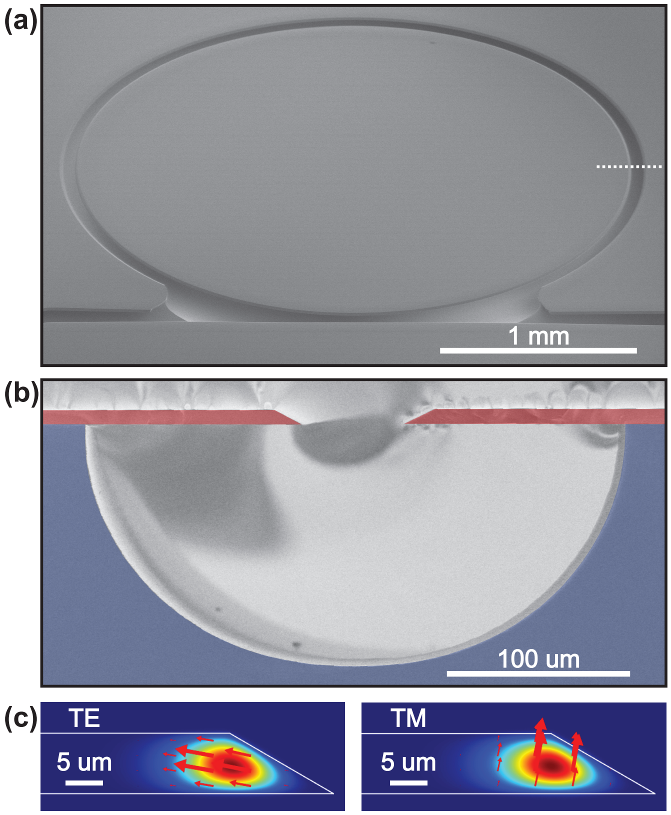

Figure 2.1: Microresonator images and mode profiles. (a) Scanning electron microscope (SEM) image of microresonator (~22 GHz FSR; 3 mm diameter). Dotted white line indicates cross section in panel b. (b) False-color SEM cross section with narrow trench structure and 120 μm undercut. (c) Left (right) panel, fundamental TE (TM) mode electrical field distribution from numerical simulation. Arrows indicate electric field vectors.

wet-etch-defined silica trenches are narrowed as illustrated in Fig. 2.1(a,b). This lowers dry-etch time for silicon removal and thereby reduces unintended microscopic silica dry etching. The temperature of each fabrication step is also strictly controlled within a $\pm 0.5^\circ C$ range. This includes both the dry etcher temperature and the XeF_2 source temperature, both of which are servo controlled to ensure reproducible results. The importance of this latter temperature control is that it permits a more precise determination (and maximization) of silicon undercut so as to completely remove silicon residue at the bottom side of the disk. Such control is also believed to minimize bottom-side surface roughness, which is an important source of loss in current resonator configurations [70]. The ultimate limit of undercut is determined by silica buckling [71]. Finally, the silica microresonators are annealed 2-3 times for 20 hours in an ultra-pure nitrogen ambient at $1000^\circ C$ to remove water and to

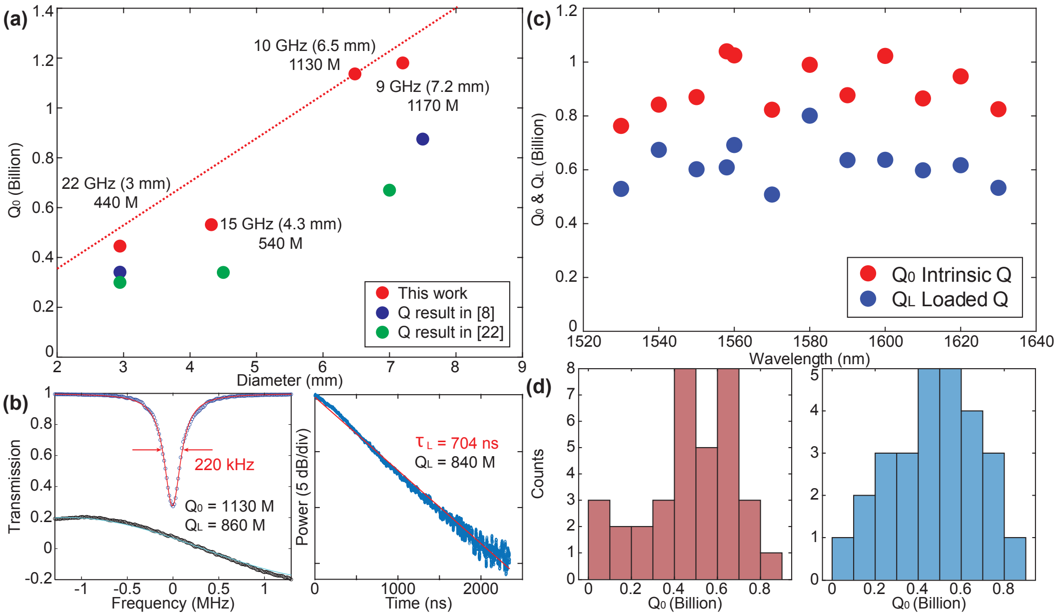

Figure 2.2: Q measurements. (a) Measured intrinsic Q_0 versus resonator diameter. FSR, resonator diameters, and Q_0 values are indicated. Red dotted line corresponds to a finesse of 60,000. (b) Left panel: resonance linewidth measurement of a 10 GHz FSR device at 1585 nm. Upper trace is resonance transmission (blue dots) with Lorentzian lineshape fitting (red curve). The linewidth is 220 kHz, corresponding to an intrinsic $Q_0 = 1.1$ billion and loaded $Q_L = 860$ M. Lower trace is a frequency calibration (black dots) from a Mach-Zehnder interferometer (FSR is 5.979 MHz) with sinusoidal fitting (cyan curve). Right panel: ring down measurement (blue) of the device measured in the left panel. An exponential decay fitting is shown in red. Photon lifetime is 704 ns, corresponding to loaded $Q_L \approx 840$ M. (c) Intrinsic Q_0 and loaded Q_L data measured from 1530 nm to 1630 nm. (d) Distribution of Q_0 values measured from different mode families for TE (left panel) and TM (right panel) mode polarization measured in a single FSR.

release bulk stress in the suspended silica structure.

Intrinsic Q factors (Q_0) are measured by characterization of resonance linewidths (accounting for waveguide loading effects) and through cavity ring down measurements. Coupling to the resonators used a tapered fiber coupler [61] and a polarization controller was used to excite modes that are primarily TE or TM like (see Fig. 2.1(c)). As an aside on the optical coupling, mechanical vibrations are present on the tapered fiber coupler. To suppress these vibrations it is possible to place the tapered fiber on the top of the wedge edge in contact with the silica surface. As a result, the coupling condition becomes stable without inducing much scattering loss to the resonator. At the same time, the amount of coupling can be readily

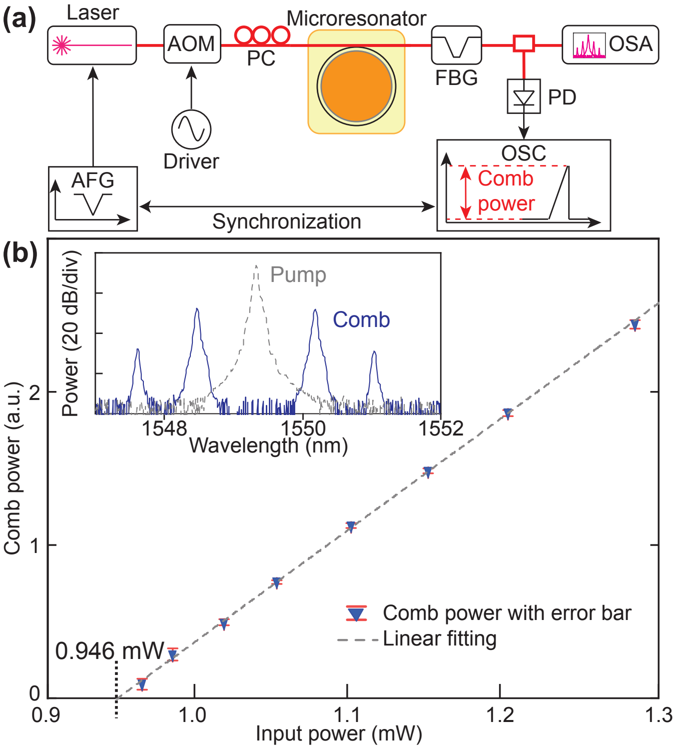

Figure 2.3: Sub-milli-Watt parametric oscillation threshold measured in device having a 9 GHz FSR. (a) Experimental setup. AOM: acousto-optic modulator, PC: polarization controller, FBG: fiber Bragg grating filter, PD: photo detector, OSA: optical spectrum analyzer, OSC: oscilloscope, AFG: arbitrary function generator. (b) Plot of parametric oscillation power versus input power (1550 nm) showing oscillation threshold of 0.946 mW. Inset: parametric oscillation spectrum (solid blue) and filtered pump (dashed gray) at 1.12 mW input power.

controlled by simply moving the contact location of the taper on the resonator. This has the effect of adjusting the distance between the taper waveguide and the location of the optical mode (see Fig. 2.1(c)) to thereby adjust the resonator loading by the waveguide.

Fig. 2.2(a) plots the highest intrinsic Q-factors obtained for several device diameters. Two device diameters have Q factors over 1.1 billion. A typical spectral measurement is illustrated in the left panel of Fig. 2.2(b), which shows a transmission spectrum for a device having a free-spectral-range (FSR) of approximately 10 GHz (diameter 6.5 mm). The full-width-at-half-maximum linewidth is measured (at 1585 nm) to be 220 kHz, corresponding to a loaded Q factor $Q_L = 860$ M. By measuring the transmission depth, a coupling Q factor of $Q_c = 3.6$ billion is determined from which an intrinsic $Q_0 = 1.1$ billion is inferred (note: $1/Q_L = 1/Q_0 + 1/Q_c$). The rising dependence of intrinsic Q factor with increasing resonator diameter has been previously observed in the wedge resonator structure and results from round trip loss that is limited by surface scattering [24, 70]. To further confirm the Q results, ringdown of cavity power was also performed. Ring down data from the same device measured in the left panel of Fig. 2.2(b) is shown in the right panel of Fig. 2.2(b). The ringdown decay gives a photon lifetime of about 704 ns, which corresponds to Q_L = 840 M in close agreement with the linewidth-inferred loaded Q. To the authors' knowledge, these are the highest optical Q factors reported for on-chip devices. In particular, previous high performance results for silica resonators are also plotted as blue and green points in Fig. 2.2(a) [24, 72]. It is also worth noting that the $Q_0 > 1$ billion performance has been maintained for more than half a year to date by enclosing the resonators in a purged plexiglass box. The devices possess ultra-high-Q over a broad spectral band as shown in Fig. 2.2(c) where measured intrinsic and loaded Q factors in a 9 GHz FSR resonator (diameter 7.3 mm) are plotted versus wavelength.

In a typical resonator, there are dozens of modes from different mode families and polarizations that have ultra-high-Q factors. Histograms of measured Q_0 values for TE (left panel) and TM (right panel) mode families in a 9 GHz FSR resonator (near 1550 nm) are plotted in Fig. 2.2(d). Q-factors in the histograms are measured by linewidth fitting on spectra taken by fast frequency scanning of an external-cavity diode laser. The scan was intentionally performed from blue to red wavelengths so that resonator thermal hysteresis effects [73] would tend to degrade the apparent Q factor. As a result, the measured Q values are likely somewhat lower than the actual Q values.

To further confirm the Q measurements, parametric oscillation threshold was also measured using the experimental setup in Fig. 2.3(a). As shown in Fig. 2.3(b), a sub-milliwatt threshold (0.946 mW) was measured using a 9 GHz FSR device at 1550 nm. This is a record low threshold for this low FSR [72]. To perform this measurement the pump line was filtered using a fiber Bragg grating as shown in the setup. The pure frequency comb power was then measured and plotted. The inset to Fig. 2.3(b) shows both the filtered and unfiltered spectrum at 1.12 mW input power.

In summary, by optimizing fabrication methods and recipe parameters, we have demonstrated a record on-chip Q-factor over 1.1 billion in silica microresonators. Future efforts will be directed towards implementing these improvements in fully-waveguide-integrated ultra-high-Q resonators [32]. Moreover, besides pure silica structures, there is significant progress in ultra-high-Q structures where silica provides the cladding for low confinement silicon nitride waveguides [13, 28, 74]. In these structures, it is important to understand loss limits imposed by silica on the overall design. More generally, the results presented here establish an upper bound for optical loss in structures using thermally grown silica.

More numbers

Finesse achieved in this chapter work is

$$\mathcal{F} = \frac{\mathrm{FSR}}{\Delta\nu} = \frac{\mathrm{FSR} \cdot Q}{\nu} = \frac{\lambda}{n\pi}\frac{Q}{D} \approx 60,000 \tag{2.1}$$

Optical propagation loss achieved in this chapter work is

$$\alpha \text{ [dB/km]} = 4343 \times \frac{2\pi n}{\lambda Q} = 21.8 \text{ dB/km} \tag{2.2}$$

Chapter 3

SURFACE SCATTERING AND OH ABSORPTION: LIMITING FACTORS

[2] Abstract

Thermal silica is a common dielectric used in all-silicon photonic circuits. Additionally, bound hydroxyl ions (Si-OH) can provide a significant component of optical loss in this material on account of the wet nature of the thermal oxidation process. A convenient way to quantify this loss relative to other mechanisms is through OH absorption at 1380 nm. In this chapter, using ultra-high-quality factor (Q-factor) thermal-silica wedge microresonators, the OH absorption loss peak is measured and distinguished from the scattering loss baseline over a wavelength range from 680 nm to 1550 nm. Record-high on-chip resonator Q-factors are observed for near-visible and visible wavelengths, and the absorption limited Q-factor is as high as 8 billion in the telecom band. Hydroxyl ion content level around 2.4 ppm (weight) is inferred from both Q measurements and by secondary ion mass spectroscopy (SIMS) depth profiling.

High-Q integrated resonators have become an essential component in nonlinear photonics. Most often, the guided light in these structures has a significant fractional overlap with silica (e.g., all-silica wedge resonators [24, 33] and silica-clad ultra-low-loss silicon nitride waveguides [13, 36]). It is therefore important to understand the loss limits imposed by the silica used in silicon photonic processing. Besides interface scattering loss, optical absorption from bound hydroxyl ions (Si-OH) can be a significant component of loss [55], especially since thermal silica is prepared using a process involving water. Bound hydroxyl ions produce a well-known fundamental absorption peak at 2720 nm [75] and the overtone at 1380 nm is used in this chapter to measure OH absorption loss in ultra-high-Q thermal-silica wedge microresonators. Further comparison to scattering loss is made over a wavelength range from 680 nm to 1550 nm. Also, using cavity-enhanced photo-thermal spectroscopy [55] near the 1380 nm band, the OH ion content level is estimated to be 2.4 ppm (weight). This

---

[2] Work presented in this chapter has been published in "Hydroxyl ion absorption in on-chip high-Q resonators," *Optics Letters* **48**, 3511-3514 (2023) [56]

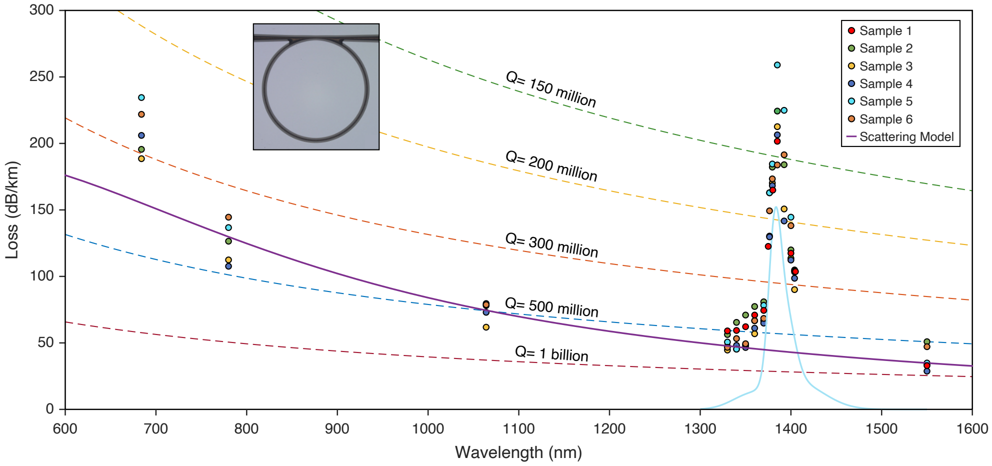

Figure 3.1: Optical loss measured from 680 nm to 1550 nm reveals the existence of the OH absorption peak near 1380 nm. The data are obtained by optical Q-factor measurement. The purple solid line is the predicted loss from surface-roughness scattering (see text). The light blue solid line is the estimated OH absorption loss in 1380 nm band (corresponding to 2.4 ppm weight). Dashed contours correspond to different Q-factor values. Inset: typical optical micrograph of the optical resonator used in the measurements.

value also agrees with Secondary Ion Mass Spectroscopy (SIMS) depth profiling performed on the resonator material. Outside of the 1380 nm band, scattering loss is confirmed by measurement and modeling to be the dominant loss mechanism in the samples tested.

Thermally-grown silica wedge whispering-gallery resonator devices were prepared as measurement samples, and featured 8 μm thermal oxide thickness with resonator diameter 6.5 mm (10 GHz free spectral range, FSR). The fabrication steps are detailed in reference [33] and a photo micrograph of a typical resonator is the Fig. 3.1 inset. The thermal silica was grown from float-zone (low background doping level) silicon wafers using the wet oxidation method. As a final step, the devices were annealed for 18-hours at 1000°C in N_2. The samples were stored and measured in a dry N_2 environment to minimize environmental impact on optical loss. Tapered fiber couplers [61, 62] were used to couple probe light to the resonator samples.

Fig. 3.1 summarizes the optical loss measurements using six of these devices measured at wavelengths from 680 nm to 1550 nm. All resonators feature intrinsic quality factor (Q-factor) over 500 million at 1550 nm. The corresponding Q-factors are also given in the plot (dashed contours). Significantly, the devices have record-high Q values for on-chip devices in the shorter wavelength bands: 300 million at

685 nm, 500 million at 780 nm, and 600 million at 1064 nm. As an aside, the loss per unit length α (dB/km) is determined from the optical Q-factor measurement using the relationship $\alpha = 4343 \times \frac{2\pi n_g}{\lambda Q_0}$ (dB/km), where Q_0 is intrinsic Q-factor in billions, n_g is the group refractive index and λ is the wavelength (nm). The intrinsic Q-factor Q_0 is obtained from the relationship $1/Q_0 = 1/Q_L - 1/Q_c$ by measuring the resonance linewidth with Lorentzian lineshape fitting to obtain the loaded Q-factor Q_L followed by measurement of transmission depth to infer the coupling Q-factor Q_c.

A strong increase in loss near 1380 nm is apparent in all six samples, corresponding to the OH absorption band and reaching over 200 dB/km. This absorption quickly decreases for wavelengths above and below 1380 nm. The loss in other spectral regions is believed to be dominated by Rayleigh scattering. The wavelength dependence of this scattering within the resonator mode volume would scale approximately as λ^{-4}, and does not fit the data. Modeling of surface scattering is described in the Methods and provides better agreement with the wavelength dependence. This theoretical dependence is given by the purple curve (for the fundamental TE mode) where surface roughness variance (1.9 nm) and correlation length (350 nm) are assumed in the plot [76]. The origin of the increased loss at the shortest wavelengths measured is not known, but possibilities include absorption loss from metallic ion impurities and scattering from material density fluctuations. For example, SIMS data has shown that Chromium is a residual contaminant in our processing, and Cr^{3+} ions can contribute 1.6 dB/km/ppbw at 800 nm (peak at 625 nm) to absorption [77].

Material	1385 (dB/km)	1550 (dB/km)
thermal silica in this study	152	3.2
1 ppmw OH in silica [75]	62.7	
Wet fiber studied in [75]	48500	100
Fiber studied in [78]	1.172	0.045
low-OH fiber [4, 5]	0.05	0.02

Table 3.1: Summary of **absorption loss rates** at both 1385 nm and 1550 nm from Fig. 3.2 and taken from the literature. Note that ppmw is parts per million in weight (equivalently, μg/g).

Cavity-enhanced photothermal spectroscopy (CEPS) [55] was used to further study the OH absorption loss. This method measures the microresonator resonance thermal triangle formation induced by the thermo-optical effect [73] to determine mode

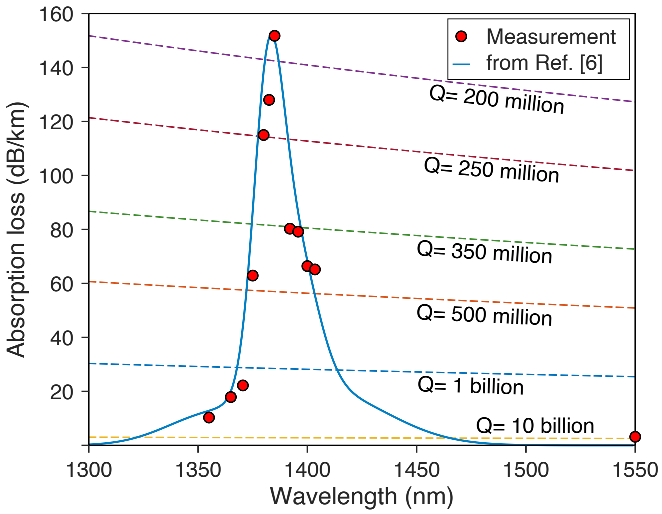

Figure 3.2: Absorption loss measurement results. Absorption loss as measured by cavity-enhanced photothermal spectroscopy in the 1380 nm band. Red dots: data from Sample 1 in Fig. 3.1. Blue solid line: 2.4 ppm (weight) OH content level absorption lineshape based on reference [75].

volume absorption. Details on this method are provided in reference [55]. Fig. 3.2 summarizes the wavelength dependence of the measured absorption loss in both the 1380 nm band and at 1550 nm. The measured absorption near 1380 nm follows reasonably well the OH overtone lineshape in silica as determined elsewhere [75] (blue curve superimposed in plot). To fit the magnitude of the lineshape function to the data, an OH content level of 2.4 ppm weight is used. Also, the data near 1550 nm indicates that by further reduction in scattering loss, the existing thermal silica can provide absorption limited Q factors as high as 8 billion. This value is 2× larger than measured for wedge resonators in a previous study [55] and is attributed to application of an improved resist cleaning step. The absorption loss measurement results at 1385 nm and 1550 nm are summarized in Table 3.1 and compared with values from the literature. The measured absorption ratio $\alpha(1385\text{ nm})/\alpha(1550\text{ nm})$ in the current data is more consistent with the report in ref. [12]. The high OH concentration in ref. [6] could possibly account for this difference.

To further confirm the OH ion impurity level and also study its spatial distribution over the resonator oxide thickness, secondary ion mass spectroscopy (SIMS) depth profiling [79] was employed (see Fig. 3.2). The absolute OH ion concentration in this measurement is obtained from the ratio $^{17}\text{OH}/^{30}\text{Si}$, as calibrated against reference samples [80, 81]. The OH concentration remains nearly constant along the depth direction with a value in reasonable agreement with the CEPS results in

Fig. 3.2. This uniformity is believed to result from diffusion-driven equilibrium [78] during the long oxide growth process and the post high-temperature annealing process [33]. The higher OH concentration near the surfaces is consistent with the hydrophilic nature of silica causing water to be adsorbed on the surfaces [51, 82, 83].

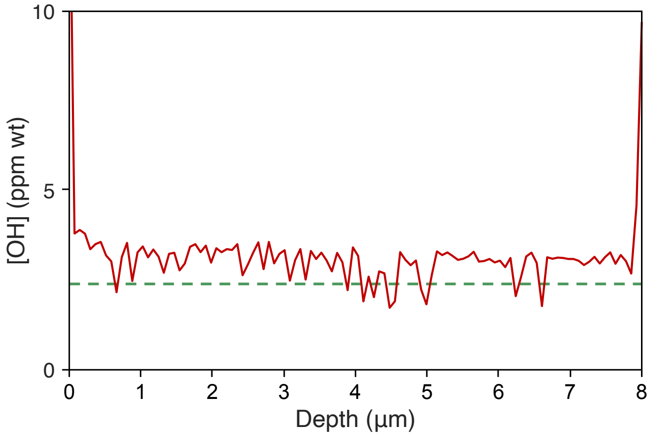

Figure 3.3: OH ion depth distribution measured using secondary ion mass spectroscopy (SIMS) over the resonator thickness (Sample 1 in Fig. 1). Dashed line indicates 2.4 ppmw level inferred from data in Fig. 3.2.

In summary, using thermal silica wedge microresonators and by measuring optical loss from 680 nm to 1550 nm, the OH ion absorption peak in 1380 nm band stands out from base line scattering loss. Absorption-only loss in the 1380 nm band was also measured using cavity enhanced photo-thermal spectroscopy. This gave a maximum absorption loss of 152 dB/km at 1385 nm. Fitting of the absorption spectrum gives an OH content level of 2.4 ppm weight, which is consistent with separate measurements performed on the resonator oxide by Secondary Ion Mass Spectroscopy. Outside the OH overtone absorption band, surface scattering was determined to be the dominant loss mechanism. Record high Q factors (limited by scattering) were measured for visible and near-visible wavelengths. Also, with further reduction scattering loss, Q values approaching 8 billion are feasible at 1550 nm. This value is higher than determined in previous measurements [55]. Overall, this investigation highlights the potential for even lower loss levels and higher Q factors using thermal silica in photonic devices.

3.1 Calculation of surface scattering loss for wedge resonators

The scattering loss for silica wedge resonators is dominant by surface inhomogeneity scattering rather than bulk inhomogeneity scattering, as evident by the following two experimental observations. First, the optical loss is roughly inversely proportional to the bending radius [33], a characteristic feature for surface roughness scattering [51, 84]. Second, with bending radius over 1 mm, the resonances of wedge resonators never have splitting effect [85] even with Q-factor over 1 billion [33].

Surface scattering loss can be modeled as dipole radiation of surface inhomogeneities polarized by the local electrical field [76]. The equivalent current density induced by the corresponding dipole moments is

$$\vec{J}(\vec{r}) = -i\omega\epsilon_0(n_0^2 - n_1^2)\vec{E}(\vec{r})$$

where ω is the angular frequency of the light, ϵ_0 is the free space permittivity, n_0, n_1 are refractive indices of cavity and cladding materials, and $\vec{E}(\vec{r})$ is the local electrical field. The corresponding radiation field and Poynting vector are given by

$$\vec{A}(\vec{r}) = \frac{\mu e^{in_1k_0r}}{4\pi r}\oint e^{-in_1k_0\hat{r}\cdot\vec{r'}}J(\vec{r'})h(\vec{r'})dS'$$

$$\vec{S}(\vec{r}) = \hat{r}\frac{\omega n_1k_0}{2\mu}|\hat{r}\times\vec{A}(\vec{r})|^2$$

where k_0 is the wave number of the light and $h(\vec{r})dS$ is the volume element of inhomogeneity. When adding up the radiation field from different parts of surface, their coherence is limited by the correlation length. Using the correlation function of surface roughness $\langle h(x)h(y)\rangle = \sigma^2R(\frac{x-y}{B})$, and assuming that the correlation length B is small enough to ignore the variation of the field within this length, the Poynting vector field can be reduced to

$$\vec{S}(\vec{r}) = \hat{r}\frac{\mu\omega n_1k_0}{2(4\pi r)^2}\sigma^2B^2\oint|\vec{J}(\vec{r'})\times\hat{r}|^2\tilde{R}[\vec{\beta}(\vec{r'}) - n_1k_0\hat{r}_{||}(\vec{r'})]dS'$$

where $\tilde{R}(\vec{k})$ is Fourier transformation of $R(\vec{x})$, $\vec{\beta}(\vec{r'})$ is the propagation constant of cavity mode at $\vec{r'}$, and $\hat{r}_{||}(\vec{r'})$ is the component of $\hat{r}$ parallel to the surface at $\vec{r'}$.

In the calculation of $\vec{S}$ and the radiation power, the parameters of the cavity mode, such as mode profiles and propagation constants, are acquired by numerical simulation (Lumerical MODE). The mode used for calculating the purple curve in Fig. 3.1 is the fundamental TE mode. The correlation function of surface roughness in the calculation is assumed to be a Gaussian function with the form $R(\frac{x-y}{B}) = \frac{1}{B\sqrt{2\pi}}e^{-\frac{(x-y)^2}{2B^2}}$. The parameters of the surface roughness are acquired by Atomic Force Microscopy (AFM) measurements, fitted with Gaussian-type function, revealing that the lower surface has σ of 2 nm, whereas the upper and wedge surfaces have σ smaller than 0.5 nm [24, 70].

Chapter 4

25-MICRON-THICK THERMAL SILICA WEDGE MICRORESONATORS

[3] Abstract

Very thick thermally grown silica layers on silicon wafers (up to 25 μm) are an important starting backbone material for weakly confined ultra-low-loss waveguides as under cladding. In this chapter, we fabricated monolithic wedge microresonators using 25 μm thick thermal silica and more than 60 million Q factors were demonstrated. The wedges were perfectly formed by advanced fabrication technology. This is the first time such a thick on-chip optical microresonator device has been made and such a thickness improves the resonance thermal stability by 6 times for device operation. Although over 1 million times more Boron dopant are present in the material, the absorption limited Q factor Q_{abs} of 5 billion is measured. Such a thick on-chip wedge structure with the ability to modify vertical dimension will also benefit application such as PIC 3D integration.

For ultra-low-loss waveguides [13, 36, 37], the under-cladding layer is critically important. The very thick thermally grown silica layers on silicon wafers (up to 25 μm) are essential as starting material because a large distance between the waveguide core and Si substrate is required to isolate the mode light from Si. To characterize such a material's optical property, one of the best methods is to make a optical resonator out of it to measure its resonance property. In this chapter, we fabricated monolithic wedge microresonators using 25 μm thermally grown silica and more than 60 million Q factors were demonstrated. The on-chip wedge structures were perfectly formed by advanced fabrication technology, confirmed by SEM cross section measurements.

The previous thermal silica wedge whispering-gallery microresonator demonstrations usually feature 8 μm thickness [24, 33, 72] mainly in consideration of procedure feasibility because of the slow growth rate of thermal oxidation (8 μm/10 days). To start device fabrication, the layout patterns are designed to have diameter

---

[3] Work presented in this chapter has **not** been published yet.

of 8.6 mm on wafer, which corresponds to 7.5 GHz free spectral range (FSR). The device fabrication starts from 25 um thermal oxidation of silicon wafers (4 inch, 1 mm thick). The thermal silica layer is of high quality and both wafer in-plane uniformity and surface uniformity is less than 0.5%. The resist patterns are formed using stepper projection lithography (projection ratio 5×). After resist development, hours-long buffered HF wet etch is implemented to form wedge structure, which leverages the photoresist peel-off effect [86]. The wedge angle can be tuned by changing the adhesion between the photoresist and the thermal silica surface. The silicon isotropic undercut etch is implemented using ICP-RIE plasma etch. High temperature (1000°C) annealing is implemented at the wafer level for hours long. The wafer is diced into 25 chips for device singulation. The device cross section SEM is shown in Fig. 4.1.

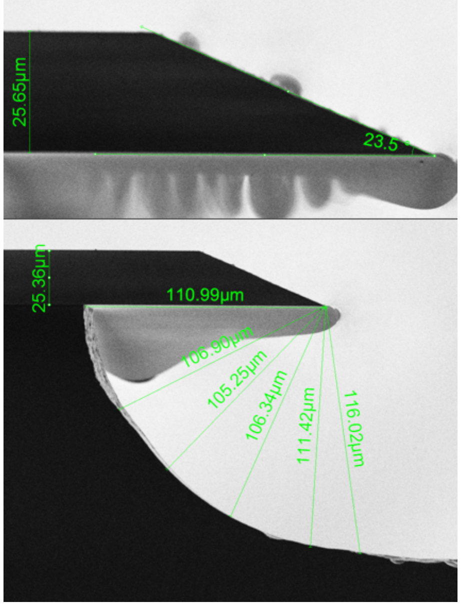

Figure 4.1: SEM cross sections of the 25 μm thermal silica wedge microresonator. Perfect wedge structure is formed by buffered HF wet etch with wedge angle 23.5°. 110 μm Si undercut is implemented using ICP-RIE plasma etch.

The device is probed using fiber taper coupler and near critical coupling condition can be achieved. As shown in Fig. 4.2, 43 million loaded Q factor Q_L is measured, and from which, 62 million intrinsic Q factor Q_0 is inferred assuming an under-coupled condition.

The absorption limited Q factor Q_{abs} is measured using cavity enhanced photothermal spectroscopy (CEPS) [55] and 5 billion Q_{abs} is obtained, which corresponds to 5.1 dB/km absorption loss. This number is close to the number obtained in 8 μm

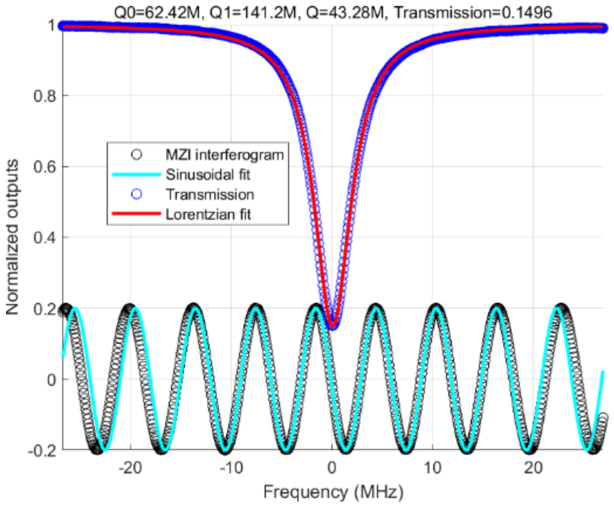

Figure 4.2: Resonance transmission linewidth measurement of a 7.5 GHz FSR device at 1550 nm

thermal silica grown from float-zone silicon wafers [56]. It's worth noting that the current wafers (resistivity < 0.03 Ω·cm) have over 1 million times increase in Boron dopant level compared with float-zone silicon wafers (resistivity > 10000 Ω·cm), which indicates reasonable amounts of Boron dopants do not contribute appreciable absorption loss.

The increased structural thermal conductivity and thermal capacity significantly improve the resonance thermal stability. The differential resonance frequency shift per unit input pump power from thermal-optical effect [73] is measured to be 1.05 MHz/mW, which is $1/6$ of the 8 μm devices.

In summary, 25 μm thermal silica wedge microresonators are demonstrated with over 60 million Q-factor and 5 billion absorption limited Q factor. Compared with 8 μm devices [33, 70], 25 μm thickness features much better resonance thermal stability and therefore reduced thermal refractive noise (TRN), which benefits many applications such as chip-based narrow-linewidth lasers [87], microwave generation [88] and on-chip reference cavities [12, 25]. Such a thick on-chip thermal silica wedge structure will enable vertical dimension possibilities on photonic integrated circuits (PIC) and benefit application such as optical waveguide 3D integration [89, 90].

Chapter 5

SOLITON MICROWAVE SOURCES USING THERMAL SILICA WEDGE RESONATORS AND DISPERSIVE-WAVE INDUCED NOISE LIMITS

[4] Abstract

Compact, low-noise microwave sources are required throughout a wide range of application areas including frequency metrology, wireless-communications, and airborne radar systems. And the photonic generation of microwaves using soliton microcombs offers a path towards integrated, low noise microwave signal sources. In these devices, a so called quiet-point of operation has been shown to reduce microwave frequency noise. Such operation decouples pump frequency noise from the soliton's motion by balancing the Raman self-frequency shift with dispersive-wave recoil. In this chapter, we explore the limit of this noise suppression approach and reveal a fundamental noise mechanism associated with fluctuations of the dispersive wave frequency. At the same time, pump noise reduction by as much as 36 dB is demonstrated. This fundamental noise mechanism is expected to impact microwave noise (and pulse timing jitter) whenever solitons radiate into dispersive waves belonging to different spatial mode families.

Soliton mode locking in optical microresonators is receiving intense interest for chip-scale integration of frequency comb systems [11]. Apart from frequency comb applications, the microwave signal produced by detection of the microcomb output is, itself, potentially important as a new microwave signal source (see Fig. 5.1). However, mode locking of microcombs at microwave rates is challenging on account of their unfavorable pump power scaling with repetition rate [58]. Indeed, only ultra-high-Q discrete silica and crystalline devices were initially able to operate efficiently at microwave rates [31, 58, 72, 91]. Nonetheless, new generations of integrated ultra-high-Q resonators are emerging that both access the microwave-rate realm [13, 32, 92] and offer more complete integrated functionality [13, 93]. Because of their superior phase noise performance compared to other miniature

---

[4] Work presented in this chapter has been published in "Dispersive-wave induced noise limits in miniature soliton microwave sources," *Nature Communications* **12**, 1442 (2021) [88]

photonic microwave approaches [28, 30, 94, 95], these devices are stimulating interest in miniature stand-alone soliton microwave sources.

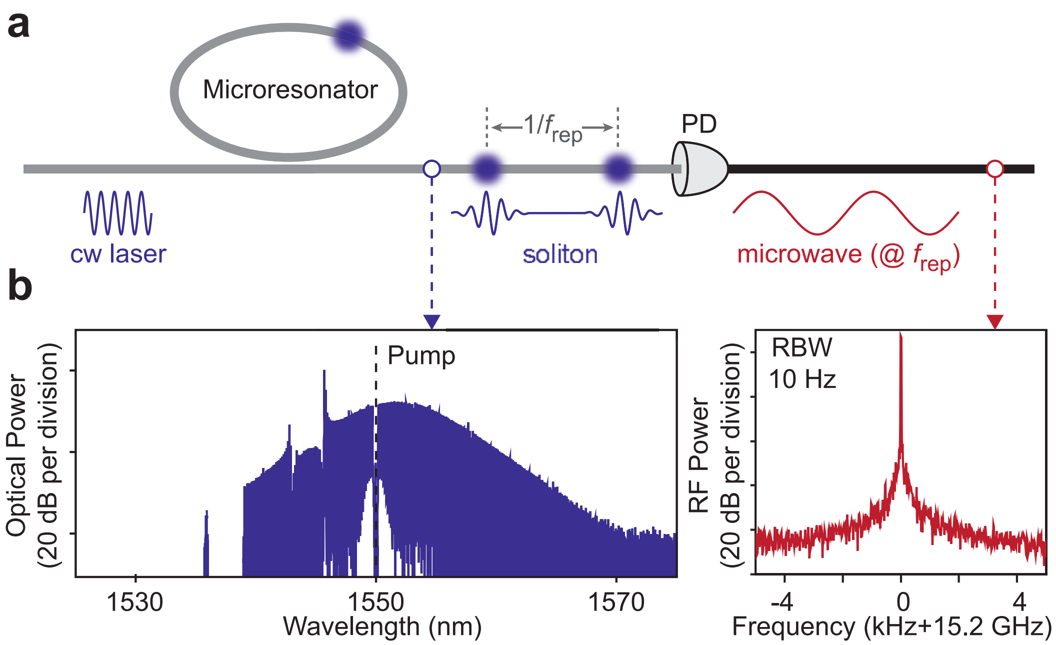

Figure 5.1: Soliton microcombs as microwave signal sources. (a) Apparatus for microwave signal generation using a soliton microcomb. A microresonator pumped by a continuous-wave (cw) laser emits a repetitive soliton pulse train, which is directed into a photodetector (PD) to produce a signal current. (b) Representative optical spectrum of a soliton microcomb with 15.2 GHz repetition rate (left panel). The pump (black dashed line) has been attenuated by an optical notch filter. The right panel shows the corresponding microwave-rate beat signal with resolution bandwidth (RBW) of 10 Hz.

While the fundamental limit of phase noise (and equivalently timing jitter) in the detected soliton pulse stream is induced by quantum fluctuations [96, 97], in practice, phase noise is dominated by sources of a more technical origin that couple to the soliton motion in various ways. For example, the Raman self frequency shift in microcombs [98, 99] provides a mechanism for transduction of changes in the detuning frequency (difference in the frequencies of the resonator mode being pumped and the pumping laser field) into the soliton repetition rate [100]. It does this by causing a frequency shift in the center frequency of the soliton spectrum (which has an overall $sech^2$ envelope) as the pump detuning frequency is varied. Group velocity dispersion then converts these spectral shifts into changes in the soliton round-trip propagation time and hence the repetition rate. The Raman process thereby couples any fluctuation of the resonator frequency (e.g., thermorefractive noise [101–104]) or the pump frequency into microwave phase noise. Dispersive waves can also induce a spectral center shift in the Kerr soliton [100, 105]. Dispersive waves can emerge as a result of higher-order dispersion [105, 106], supermodes [107], or when solitons radiate into resonator modes that do not belong to the soliton-forming mode family. And the spectral shift they induce can offset the Raman self shift. Indeed, when dispersive wave and Raman shifts are in balance, a *quiet* operating point is attained whereby coupling of detuning frequency fluctuations into the soliton repetition rate are greatly reduced [108].

Here, by investigating possible limits in application of the quiet operating point, we report the observation of a fundamental noise source in the soliton repetition rate. Referred to as spatio-temporal thermal noise, it originates from uncorrelated thermal fluctuations between distinct transverse modes of the microresonator, and can couple into the soliton repetition rate through the formation of a dispersive wave. Theory and experiment show that the spatio-temporal thermal noise imposes a considerable limitation on the repetition rate stability of soliton microcombs emitting dispersive waves into spatial mode families that are distinct from the soliton-forming mode family. Beyond the study of the dispersive-wave noise, a convenient way to operate the soliton microwave source at the quiet point while also disciplining it to an external reference, such as a clock, is demonstrated.

5.1 Soliton generation in thermal silica wedge microresonators

A silica disk microresonator with intrinsic Q factor exceeding 300 million and free-spectral-range (FSR) around 15 GHz is used in the study [24, 33]. The microresonator is packaged with active temperature stabilization [64] and operated under an acoustic shield to block environmental perturbations (Fig. 5.2a,b). By continuously pumping the resonator with an amplified fiber laser, bright soliton pulses are generated, which are further stabilized by servo control of the pump laser frequency with respect to the average soliton power [109]. The residual error in the feedback loop is monitored by an electrical spectral analyzer. The soliton beatnote is photodetected and characterized using a phase noise analyzer and a frequency counter. The beatnote of the soliton microcomb shows a 15.2 GHz repetition rate (see Fig. 5.1). Its phase noise exhibits a smooth spectral shape across a wide frequency range as a result of isolation provided by the package and acoustical shield (Fig. 5.2b). As a benchmark of the stability, the fractional Allan deviation of the beatnote is plotted in Fig. 5.2c and reaches 5.7×10^{-11} at 50 ms averaging time.

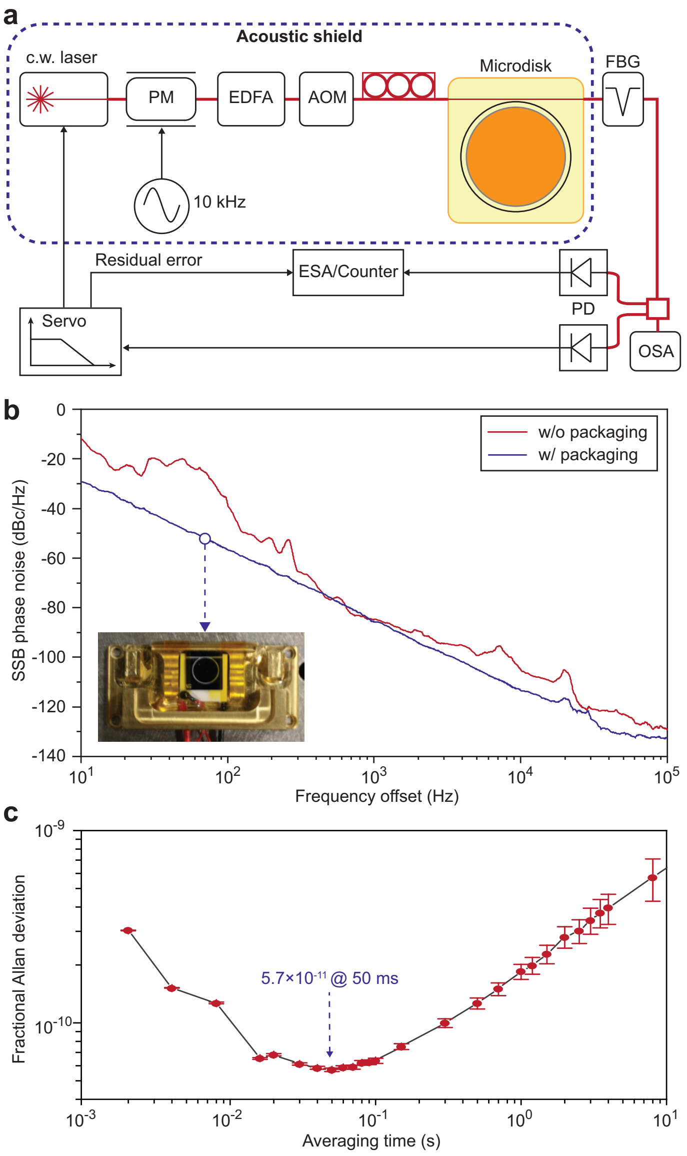

Figure 5.2: Experimental setup and preliminary microwave signal characterization.(a) Experiment setup for soliton generation. PM: phase modulator; EDFA: erbium-doped-fiber-amplifier; AOM: acousto-optic modulator; FBG: fiber-Bragg-grating notch filter; PD: photodetector; OSA: optical spectral analyzer; ESA: electrical spectral analyzer. (b) Typical phase noise spectrum of detected soliton pulse stream (scaled to 15.2 GHz) obtained using packaged/unpackaged microresonators. Inset: photo of a packaged microresonator. (c) Fractional Allan deviation of soliton pulse rate.

5.2 Quiet point operation

Plotted in Fig. 5.3a is a representative optical spectrum of the soliton microcomb, showing its characteristic sech^2 spectral envelope. Dispersive waves (the spectral

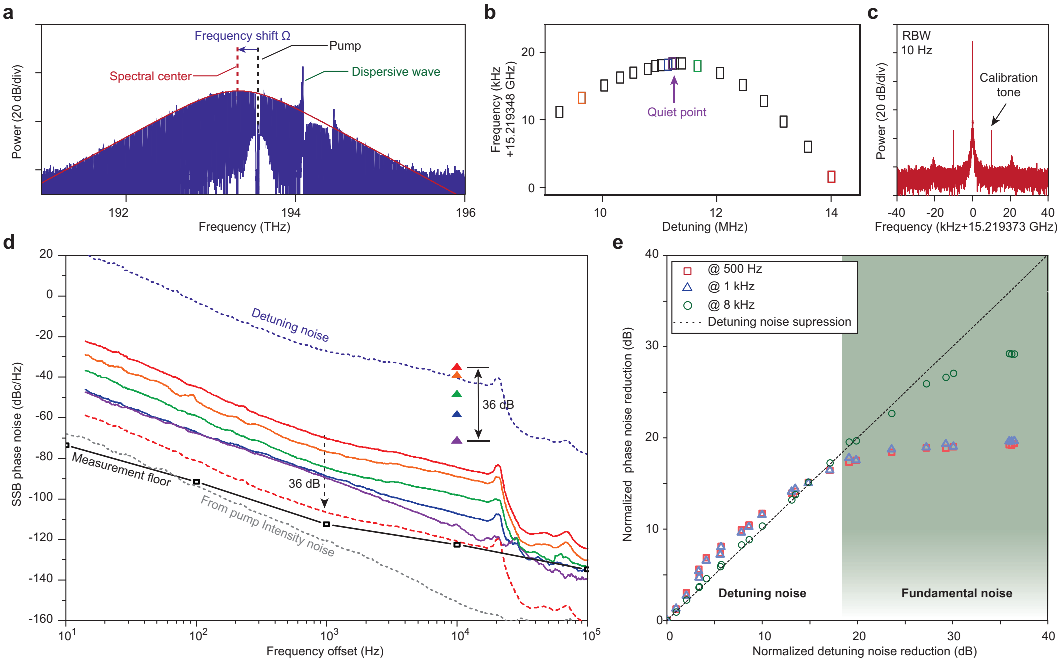

Figure 5.3: Noise spectra near and away from the quiet point. (a) Soliton optical spectrum showing spectral envelope (red solid line), the attenuated pump (black dashed line), and a strong dispersive wave. The spectral center of the soliton (red dashed line) is shifted in frequency relative to the pump frequency. (b) Measured soliton repetition rate versus laser-cavity detuning ($\delta\omega/2\pi$), where the existence of a quiet point is revealed. (c) Electrical spectrum showing soliton repetition rate. Two sidebands at 10 kHz offset frequency are induced by phase modulation of the pump and are used to calibrate the contribution of detuning noise. (d) Soliton microwave phase noise (solid curves) and calibration tone power (triangles) at different detuning frequencies (indicated by color in accordance with panel b). The optical detuning noise is the blue dotted line. At the quiet operating point, its calibration-inferred contribution to microwave noise is the dashed red curve. Noise induced by the pump intensity fluctuation (gray dotted line) is also plotted. The phase noise analyzer instrumental noise floor is shown as the black line. (e)Plot of actual noise suppression versus calibration tone suppression at several offset frequencies. The dashed line indicates the expected phase noise suppression if detuning noise is dominant.

spurs on the envelope) also appear in the spectrum and result from frequency degeneracy between comb lines and other transverse modes that do not belong to the soliton forming mode family [91, 100, 108, 110]. It is noted that the spectral envelope center of the soliton is offset from the pump frequency. This is caused by the cumulative effect of the Raman-induced soliton-self-frequency-shift (SSFS) Ω_{Raman} [98–100] and dispersive-wave induced spectral recoil Ω_{recoil} [108, 110, 111]. The soliton repetition rate, ω_{rep}, is related to these frequency shifts by [100, 108]

$$\omega_{rep} = D_1 + \frac{D_2}{D_1}(\Omega_{Raman} + \Omega_{recoil}), \tag{5.1}$$

where $D_1/2\pi$ is the FSR and D_2 is proportional to the group velocity dispersion (GVD) of the soliton-forming mode family [58, 112]. Therefore, through the respective dependence of Ω_{Raman} and Ω_{recoil} on detuning frequency $\delta\omega = \omega_o - \omega_P$ (ω_o is frequency of the cold cavity mode being pumped by optical field at frequency ω_P), the soliton repetition rate becomes a function of the detuning frequency. As reported in previous literature, noise in ω_P often plays a dominant role in causing fluctuations in $\delta\omega$, and subsequently, by way of Eq. (5.1), also in ω_{rep} [108, 113, 114]. However, it has also been shown that interplay between Raman SSFS and dispersive-wave induced spectral recoil can be used to suppress this noise transfer [108, 114]. Along these lines, Fig. 5.3b is the measured dependence of soliton repetition rate on detuning $\delta\omega/2\pi$, and shows a parabolic-like trend instead of a monotonic trend. The slope, $\beta = \partial\omega_{rep}/\partial\delta\omega$, vanishes at around 11.5 MHz detuning, corresponding to the quiet point of operation where dispersive wave and Raman induced shifts are in balance. Here, the detuning $\delta\omega$ is calculated based on equation (5.23) in Methods. By operating the soliton microcomb near this quiet point, the contribution of detuning noise to the soliton repetition rate noise can be reduced [108, 114].

To actively monitor the degree to which the detuning noise contribution is suppressed through quiet point operation, we modulate the phase of the pump laser at 10 kHz to create a large spike in the detuning noise spectrum. This induces calibration tones in the vicinity of the soliton beatnote [114], as shown in Fig. 5.3c. Measured phase noise spectra of the detected soliton microwave signal along with the power of calibration tone (see colored triangle points) are plotted in Fig. 5.3d for different detuning frequencies. As an aside, the pronounced bump around 20 kHz in the phase noise spectrum is caused by the piezoelectric tuning bandwidth of the pump laser. Away from the quiet point, the phase noise is largest and is found to follow the spectral profile of the detuning noise, which is extracted from the residual error signal in the locking loop. The contribution of the detuning noise can be scaled based on the power of calibration tone to determine its contribution in each measurement. At the quiet point, 36 dB of noise suppression is measured using the calibration tone. And the corresponding inferred detuning noise contribution (dashed orange spectrum in Fig. 5.3d) is below the actual measured noise spectrum at the quiet point (purple spectrum in Fig. 5.3d). This indicates that another noise source is

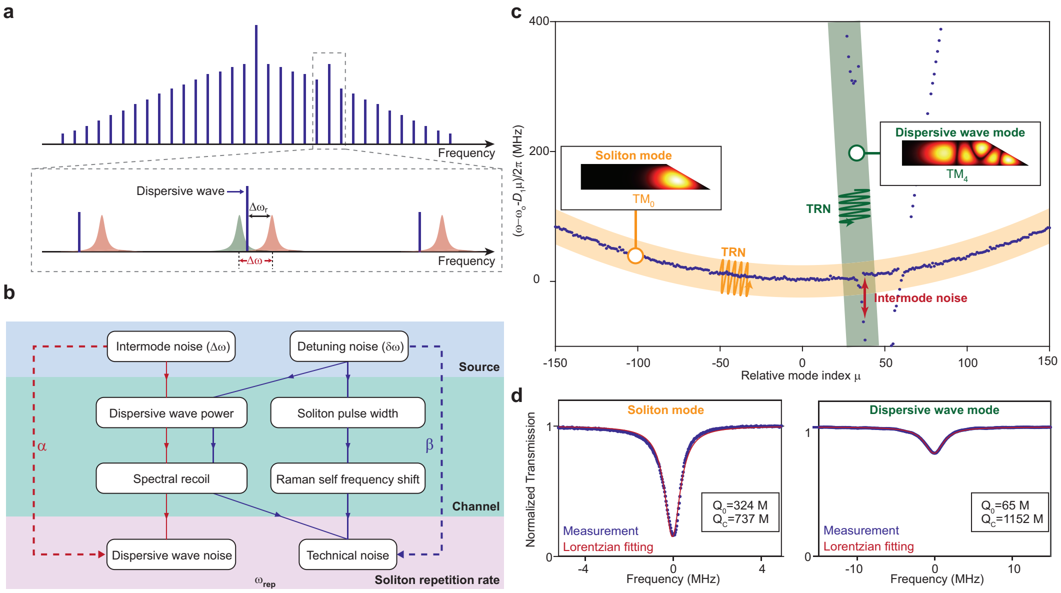

Figure 5.4: Concept of dispersive-wave-induced noise and identification of mode families. (a) Spectral relationship of soliton spectrum to dispersive wave forming mode. Blue lines indicate soliton spectral lines. Red and green shaded regions denote soliton-forming and dispersive-wave resonator modes, respectively. (b) Left side: physical steps involved in coupling fluctuations in $\Delta\omega$ (intermode noise) into soliton repetition rate. Right side: physical steps involved in coupling fluctuations in $\delta\omega$ (detuning noise) into soliton repetition rate. Noise sources (top) are transduced (α and β coupling channels) into the soliton repetition rate (bottom). Detuning noise results mainly from the pumping laser noise contributing to $\delta\omega$ and thereby causes technical noise in the soliton repetition rate. Intermode noise results from fundamental thermo-refractive noise of the dispersive wave and soliton mode frequencies contributing to $\Delta\omega$. (c) Measured mode family dispersion of the microresonator. Numerically simulated cross sections of soliton (TM_0) and dispersive wave (TM_4) modes are plotted and identified with the corresponding frequency branches. Orange and green bands (and wavy lines) are suggestive (and highly magnified) fluctuations induced by thermo-refractive noise (TRN). (d) Measured transmission spectra of soliton and dispersive wave resonator modes. The intrinsic (Q_0) and coupling (Q_C) Q-factors are extracted by fitting the Lorentzian lineshapes and transmission minima.

limiting the phase noise at the quiet point. As one possible source of this limit, pump intensity noise could also couple into the soliton repetition rate through the combined effect of Kerr and Raman nonlinearity [113, 114]. However, its contribution (see dashed gray curve in figure) is evaluated in the Methods and appears to be negligible in this measurement. Fig. 5.3e gives a comparison of the measured phase noise reduction (referenced to the highest phase noise trace) versus the reduction inferred

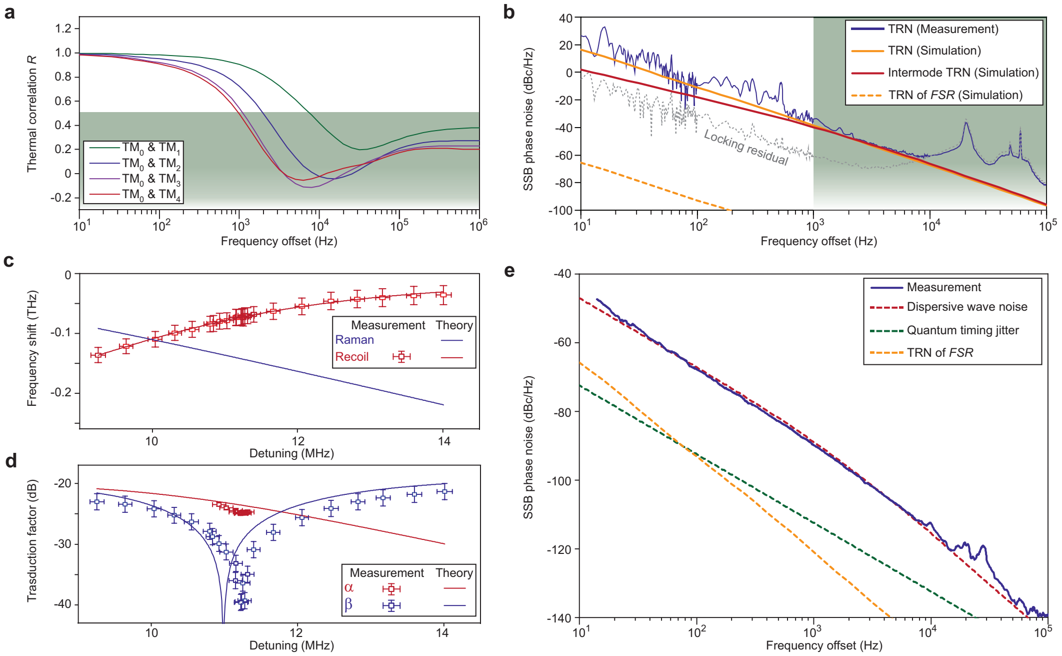

Figure 5.5: Intermode thermal noise (between dispersive wave and soliton modes) and its impact on soliton repetition rate. (a) Simulated temperature correlation R between transverse mode volumes versus frequency of thermal fluctuation. Specific transverse mode pairs are indicated in the legend. Green region corresponds to $R < 0.5$. (b) Measured and simulated TRN of a TM_0 mode. The simulated intermode TRN between TM_0 and TM_4 is also displayed. Green region corresponds to $R < 0.5$ in panel a. (c) Contribution of Raman SSFS and dispersive recoil to total spectral center frequency shift of the soliton. The error bar indicates standard deviation, and is contributed from fitting of the lineshape. (d) Measured and calculated noise transduction factors. The error bar indicates standard deviation. The error in detuning is contributed by the lineshape fitting, while the transduction factor error comes from the signal analyzer. (e) Measured phase noise at maximum quiet point suppression and calculated dispersive-wave induced noise originating from intermode TRN. Quantum timing jitter and thermorefractive noise (TRN) of the FSR are also plotted for comparison.

by the calibration tone. A clear saturation in the measured noise reduction near the quiet point is shown at several different offset frequencies, suggesting again that a new source of noise is present. The saturation is stronger at lower offset frequencies indicating that the noise mechanism is larger at lower frequencies (see Fig. 5.3d). As an aside, the quiet-point-induced phase noise reduction is also slightly higher than indicated by the calibration tone for lower noise suppression levels (when measured at 500 Hz and 1 kHz offsets). This could result from possible instrument calibration error associated with calibration using a 10 kHz tone.

5.3 Dispersive-wave induced noise

Prior analysis of fundamental sources of repetition rate noise assume that the soliton is formed and couples solely within a single transverse mode family. However, the practical need for higher Q resonators favors larger resonator cross section so as minimize the impact of interface and sidewall roughness [39]. Typically, several transverse modes besides the soliton forming mode exist in the microresonator. And when longitudinal modes in these other families experience near degeneracy with a mode in the soliton, the soliton radiates power creating a dispersive wave (Fig. 5.4a) [91, 100, 108, 110]. The radiative power depends strongly upon the degree of resonance as determined by $\Delta\omega$ (the frequency difference between the two modes), $\Delta\omega_r$ (the frequency difference between the soliton comb line and the soliton-forming mode with index r), and κ_B (the optical loss rate of the dispersive wave mode). The relationship between these difference frequencies is illustrated in Fig. 5.4a. The radiated power causes a frequency recoil, Ω_{recoil}, in the soliton spectral center relative to the pump frequency which takes the form [108]

$$\Omega_{recoil} \propto \frac{1}{(\Delta\omega')^2[(\Delta\omega_r - \Delta\omega')^2 + \frac{\kappa_B^2}{4}]}, \tag{5.2}$$

where $\Delta\omega'$ is the frequency difference between the partially hybridized crossing mode and the soliton mode, denoted by $\Delta\omega' = \Delta\omega/2 + \sqrt{\Delta\omega^2/4 + G^2}$ (where G is the coupling strength between the soliton and crossing mode). $\Delta\omega_r$ is determined by both detuning $\delta\omega$ and recoil (and thereby $\Delta\omega$). And this equation provides a way for fluctuations in $\delta\omega$ and $\Delta\omega$ to impact the soliton repetition rate. Specifically, the resulting fluctuations in Ω_{recoil} cause spectral center fluctuations of the soliton that randomly vary its round trip time as a result of second order dispersion. The physical process steps involved in this new noise transduction mechanism are depicted in Fig. 5.4b. A transduction factor $\alpha \equiv \partial\omega_{rep}/\partial\Delta\omega$ relating the repetition rate to changes in $\Delta\omega$ is defined and noted in the figure. For comparison, the process steps involved in the transduction of detuning noise into repetition rate changes (β factor defined earlier) are also provided. As noted earlier, detuning noise can be quieted through interference between the pathways indicated in Fig. 5.4b, one of which uses portions of the dispersive wave recoil process.

To identify the mode families that constitute the soliton microcomb and the dispersive wave in the experiment, we perform mode family dispersion spectroscopy using a scanning external-cavity-diode-laser (calibrated by a separate Mach-Zehnder interferometer), as shown in Fig. 5.4c. Comparing the measurement with numerical modeling of the modal dispersion, the mode family that gives rise to the strong dispersive wave in Fig. 5.3a is determined to belong to the TM_4 mode family, while the soliton is formed on the TM_0 mode family. Their Q factors are also measured, as shown in Fig. 5.4d.

Thermal noise in the dispersive wave

Fluctuations associated with thermal equilibrium result in spatial and temporal variations of temperature in the microresonator [101–104, 115]. Such temperature fluctuations, characterized by a spectral density $S_{\delta T}$ of the modal temperature fluctuations, induce a frequency fluctuation δD_1 in the resonator FSR (and in turn the soliton repetition rate) through the thermo-optic effect that is characterized by the spectral density $S_{\delta D_1}$,

$$S_{\delta D_1} = \frac{n_T^2}{n_o^2} D_1^2 S_{\delta \bar{T}}, \tag{5.3}$$

with n_T the thermo-optic coefficient and n_o the refractive index of the mode. This noise contribution to the soliton repetition rate, and that induced by quantum vacuum fluctuations [96, 97], are found to be much smaller than the measured noise in Fig. 5.3d. However, as now shown, thermorefractive noise (TRN) induced in the modes participating in dispersive-wave emission can be a major source of repetition rate noise.

From the analysis in the previous section, noise in relative frequency, $\Delta\omega$, will couple to the repetition rate through the parameter α. The TRN induced noise in $\Delta\omega$ is given by the following spectral density (see Methods),

$$S_{\Delta\omega} = \frac{n_T^2}{n_o^2} \omega_o^2 (S_{\delta T_S} + S_{\delta T_D} - 2R\sqrt{S_{\delta T_S} S_{\delta T_D}}), \tag{5.4}$$

where δT_S and δT_D give temperature fluctuations of mode volumes associated with the soliton and dispersive-wave modes involved in the definition of $\Delta\omega$. R is a frequency dependent function discussed in the Methods section that accounts for correlation between the fluctuations δT_S and δT_D. This correlation can be modeled using the finite-element-method (FEM) and the fluctuation-dissipation theorem (FDT) [103, 104, 115]. Simulation results for different pairs of transverse modes are plotted in Fig. 5.5a. On account of thermal diffusivity, the function R decreases rapidly with increasing frequency, so that beyond a thermal-limited rate the temperature fluctuations of the two modes become uncorrelated. When this happens, the value of $S_{\Delta\omega}$ exceeds $S_{\delta D_1}$ by several orders since it reflects temperature fluctuations in absolute (as opposed to relative) optical frequencies.

In order to test the numerical results and parameters used to simulate these thermally-related quantities [103, 104], we measured the TRN of the soliton mode. The frequency fluctuations of the mode were tracked by Pound-Drever-Hall (PDH) locking a fiber laser to a cavity resonance. The locked laser frequency is then measured using an optical frequency discriminator as described in the Methods. The measured single-sideband TRN is plotted in Fig. 5.5b, and is in good agreement with the simulation. The calculated phase noise of the intermode TRN using the soliton mode and dispersive wave mode is also plotted for comparison. Suppression of intermode TRN is apparent at low-offset frequencies relative to the single mode TRN. However, at higher offset frequencies (above ~ 1 kHz), the intermode TRN becomes the summation of TRN contributions belonging to each mode. The TRN of the FSR is also shown for comparison. Notice that despite the improved correlation of the intermode TRN at lower offset frequencies, it still dominates the microwave phase noise measured in Fig. 5.3d and Fig. 5.3e. This happens because the TRN noise rises very rapidly as offset frequency decreases, even overcoming the improving correlation of TRN between the dispersive wave mode and soliton forming mode.

An additional measurement of soliton microwave phase noise was performed except using PDH locking of the pump laser to the resonator as opposed to servo control using soliton power. Under these conditions, the pump frequency tracks the cavity resonance, thereby suppressing its technical noise contribution to the soliton phase noise. As expected the measured noise spectrum showed a limitation consistent with the dispersive wave noise.

A summary of noise contributions to the soliton repetition rate yields

$$S_{\omega_{rep}}(f) = \alpha^2 S_{\Delta\omega} + S_{\delta D_1} + S_Q + \beta^2 S_{\delta\omega} + S_P. \tag{5.5}$$

To evaluate the noise transduction factors, experimental results are fitted with theory based on the Lugiato-Lefever equation (see Methods). The Raman frequency shift and dispersive-wave recoil are plotted in Fig. 5.5c, where the error bar is the standard deviation contributed from fitting of the soliton spectral envelope. The frequency recoil in eqn. 5.2 is fitted in the same graph to evaluate mode coupling coefficients. Noise transduction factors α and β are then calculated and plotted in Fig. 5.5d together with the measured results. Figure 5.5e shows both measured and calculated phase noise of the soliton repetition rate while operating at the quiet point. Excellent agreement with the predicted intermode TRN induced noise is obtained by setting $\alpha = -24.5$ dB (measurement value), which is close to the theoretical value $\alpha = -23.6$ dB. Other fundamental noise contributions are also plotted, but are not limiting factors in the current measurement [96, 101–104].

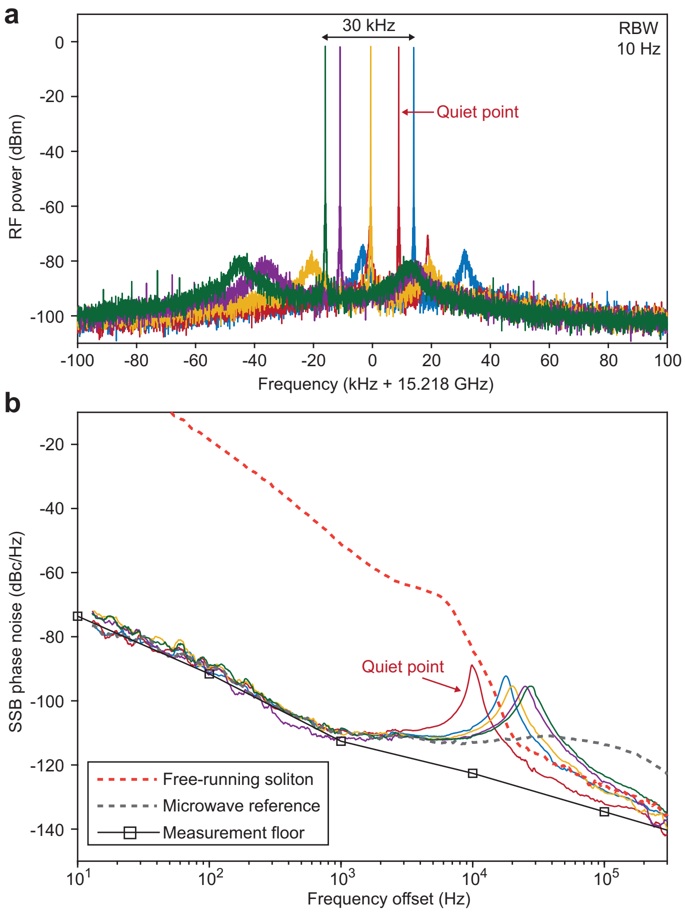

Figure 5.6: Soliton repetition rate disciplined to an external microwave source. (a) Electrical beatnote of locked soliton repetition rate showing fine tuning control of the repetition rate. The resolution bandwidth is 10 Hz. (b) Phase noise of free-running (dashed red line) and disciplined soliton microcomb (indicated by color in accordance with panel a). The trace measured near the quiet point is indicated. The phase noise of the microwave reference source is also displayed (gray dashed line).

5.4 External reference locking at the quiet point

Most signal sources provide a feature that allows the oscillator frequency to be conveniently locked to an external reference such as a clock so as to provide long term frequency stability [18]. In the present device, there is a straightforward way to achieve this locking that also provides fine tuning control of the microwave frequency near the quiet point. As a proof of concept, instead of servo controlling the soliton system by controlling the soliton power [109], we lock the soliton repetition rate to a high-performance electrical signal generator by servo controlling the optical pump frequency. The resulting soliton beatnote is shown in Fig. 5.6a, and can track the frequency of the microwave source over a 30 kHz range to achieve fine tuning control. This range is likely determined by the soliton existence range, which is, in turn, determined by the pump laser power [112]. At the same time, the soliton microwave phase noise, shown in Fig. 5.6b, is disciplined to the reference oscillator within the servo locking bandwidth. The peak around 10 kHz is induced by the servo locking bandwidth. At high-offset frequencies, the soliton phase noise outperforms the electrical oscillator (a Keysight PSG) by up to 20 dB. A variation in noise performance with fine tuning is apparent with the best performance corresponding to operation near the quiet point.

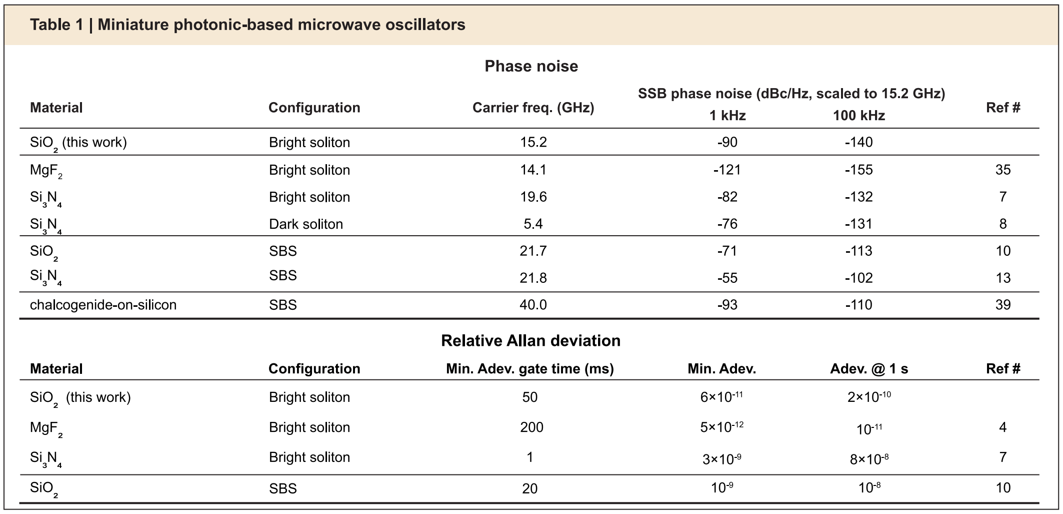

Table 1 | Miniature photonic-based microwave oscillators

Phase noise

Material	**Configuration**	**Carrier freq. (GHz)**	**SSB phase noise (dBc/Hz, scaled to 15.2 GHz)** 1 kHz	**SSB phase noise (dBc/Hz, scaled to 15.2 GHz)** 100 kHz	**Ref #**
SiO_2 (this work)	Bright soliton	15.2	-90	-140	
MgF_2	Bright soliton	14.1	-121	-155	35
Si_3N_4	Bright soliton	19.6	-82	-132	7
Si_3N_4	Dark soliton	5.4	-76	-131	8
SiO_2	SBS	21.7	-71	-113	10
Si_3N_4	SBS	21.8	-55	-102	13
chalcogenide-on-silicon	SBS	40.0	-93	-110	39

Relative Allan deviation

Material	**Configuration**	**Min. Adev. gate time (ms)**	**Min. Adev.**	**Adev. @ 1 s**	**Ref #**
SiO_2 (this work)	Bright soliton	50	6×10^{-11}	2×10^{-10}	
MgF_2	Bright soliton	200	5×10^{-12}	10^{-11}	4
Si_3N_4	Bright soliton	1	3×10^{-9}	8×10^{-8}	7
SiO_2	SBS	20	10^{-9}	10^{-8}	10

Table 5.1: Comparison of miniature reported photonic-based microwave oscillators. Performance of an on-chip silica bright soliton microcomb (this work), a Crystalline bright soliton microcomb [31, 114], a Si_3N_4 bright soliton microcomb [92], a Si_3N_4 dark soliton microcomb [13], a SiO_2 Brillouin laser [30], a Si_3N_4 Brillouin laser [28], and a hybrid electric-Brillouin oscillator [116].

In conclusion, we demonstrated a low-noise 15 GHz oscillator based on soliton microcombs. The measured phase noise of -90 dBc/Hz at 1 kHz and -140 dBc/Hz at 100 kHz offset frequencies is a record low among existing photonic-chip-based microwave sources [13, 28, 30, 92, 94, 95] (scaled to 15 GHz). A comparison of miniature photonic-based microwave oscillators is included in Table. 5.1. The low noise performance was obtained by operation near the soliton mode locking quiet point [108], where technical noise suppression as large as 36 dB was measured. Discipline of the soliton microwave source to an external microwave reference was also demonstrated, which could be useful in combination with miniaturized optical clocks [18].

A new fundamental noise mechanism associated with dispersive waves belonging to non soliton-forming mode families was also identified and theoretically modeled. Since dispersive waves induced by distinct transverse modes are ubiquitous across many soliton microcomb systems [45, 58, 92, 112, 117], this noise mechanism is expected to appear in other soliton microwave systems. Nonetheless, several methods can be implemented to mitigate this noise. First, use of dispersive waves within the same longitudinal mode family (as formed by higher order dispersion [105, 106, 118, 119]) could be investigated. In this case, better overlap of the dispersive-wave modal profile with the soliton mode would be expected to reduce the dispersive wave noise. Also, increasing the modal volume, reducing the thermo-optic coefficient or moving to cryogenic temperatures [120] could also greatly enhance the thermal stability of the microresonator [12, 31]. Such techniques might ultimately endow these photonic microwave sources with quantum-limited performance [96].

Experimental details

The resonant frequencies of the modes are measured by scanning an external cavity diode laser across a broad wavelength span (1520 nm - 1630 nm in this measurement). The laser scan is precisely measured by a radio-frequency calibrated Mach-Zehnder interferometer [58, 121]. The resonant frequency at mode index μ is expanded up to the second order with respect to the mode number μ,

$$\omega_\mu = \omega_0 + D_1\mu + \frac{1}{2}D_2\mu^2 + O(\mu^3). \tag{5.6}$$

From the measurement, the parameters of the soliton mode family are $D_{1S}/(2\pi) = 15.21857$ GHz, $D_{2S}/(2\pi) = 7.5$ kHz, and the parameters of the dispersive wave mode mode family are $D_{1D}/(2\pi) = 15.17479$ GHz, $D_{2D}/(2\pi) = 7.5$ kHz.

The soliton microcomb is amplified to around 5 mW using an EDFA before coupling into the high-speed photodetector. The phase noise of soliton repetition rate is measured using a Rohde-Schwarz FSUP26 phase noise analyzer with cross-correlation function. The soliton beatnote is down-mixed with a high-performance electrical oscillator (Agilent E8257D PSG analog signal generator) before sending into a frequency counter for the measurement of Allan deviation.

The detuning noise is obtained by monitoring the residual error signal of the locking loop. The transduction factor (slope) between error signal and pump-cavity detuning

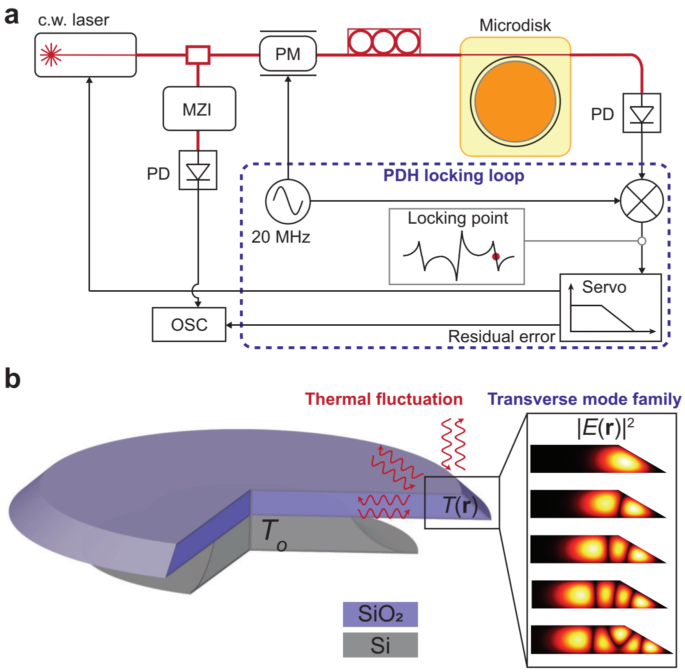

Figure 5.7: TRN measurement and resonator geometry. (a) TRN measurement setup. MZI: Mach-Zehnder interferometer. OSC: oscilloscope. PD: photodiode. PM: phase modulator. (b) Cross sectional view of the microresonator. Multiple transverse modes are supported in the suspended wedge-shaped whispering gallery. The surrounding silica, silicon, and air serve as a heat reservoirs. The ambient temperature is denoted by T_o.

is calibrated by mapping the error signal with respect to different soliton operation points. No obvious dependence of detuning noise on specific soliton operation point is observed, indicating that the detuning noise is primarily determined by the pump laser and the servo.

The TRN measurement setup is shown in Fig. 5.7a. A fiber laser is locked to a soliton forming mode using the Pound-Drever-Hall (PDH) locking technique. To mitigate the thermo-optic locking effect [73, 122, 123], the power launched into the microresonator is reduced. Also, the locking point is set to a sideband of the PDH error signal to reduce the power coupled into the microresonator. The TRN is then extracted by monitoring the laser frequency in real time using a Mach-Zehnder inteferometer as an optical frequency discriminator.

The error of the results are contributed from instrumental and fitting errors. In the phase noise measurement, the signal analyzer contributes an uncertainty of < 1 dB for 100 Hz to 10 MHz offset and < 3 dB for 1 Hz to 100 Hz and 10 MHz to 30 MHz offset. In the detuning noise measurement, the measurement uncertainty is < 3 dB. Fitting uncertainty is evaluated using nonlinear regression.

Thermal noise theory

In this section, we derive the spectral density of modal temperature fluctuation based on the Fluctuation-dissipation theorem (FDT) [103, 115, 124]. As shown in Fig. 5.7b, the microresonator exists in a heat reservoir with temperature T_o. The temperature deviation from thermal equilibrium follows the heat equation

$$\rho C \frac{\partial \delta T}{\partial t} - k\nabla^2 \delta T = \frac{\partial \delta Q}{\partial t} = T_0 \frac{\partial \delta S}{\partial t}, \tag{5.7}$$

where ρ, C, and k are respectively the material mass density, heat capacity, and thermal conductivity. δQ and δS are local fluctuation of heat and entropy. First we study the fluctuation of the optical-mode-weighted average temperature, which takes the form

$$\overline{\delta T} = \int \delta T q(\mathbf{r}) d^3\mathbf{r}. \tag{5.8}$$

Here the density $q(\mathbf{r})$ represents the normalized distribution of the electrical field intensity (Fig. 5.7b), which can be written as

$$q(\mathbf{r}) = \frac{|E(\mathbf{r})|^2}{\int |E(\mathbf{r})|^2 d^3\mathbf{r}}. \tag{5.9}$$

As described in previous literature [103, 115], to properly formulate the FDT a periodic entropy injection is applied onto the system such that

$$\delta S = F_o \cos(2\pi f t) q(\mathbf{r}). \tag{5.10}$$

The resulting time-averaged dissipation power yields

$$W_{diss} = \int \frac{k}{T_o} < (\nabla \delta T)^2 > d^3\mathbf{r}, \tag{5.11}$$

where $<>$ denotes time-averaging, which, according to the FDT, gives the single-sideband power spectral density (PSD) of $\overline{\delta T}$,

$$S_{\overline{\delta T}}(f) = \frac{\hbar W_{diss}}{\pi f F_0^2} \coth\left(\frac{\pi \hbar f}{k_B T_0}\right), \tag{5.12}$$

with k_B Boltzmann's constant.

This approach can be extended to reveal the PSD of temperature difference between two optical modes, $S_{\Delta T}$, by introducing the difference in field intensity distributions as follows:

$$q(\mathbf{r}) = q_1(\mathbf{r}) - q_2(\mathbf{r}) = \frac{|E_1(\mathbf{r})|^2}{\int |E_1(\mathbf{r})|^2 d^3\mathbf{r}} - \frac{|E_2(\mathbf{r})|^2}{\int |E_2(\mathbf{r})|^2 d^3\mathbf{r}}, \tag{5.13}$$

where E_1 and E_2 represent the respective electrical fields of the two modes. From these results, the spectral density of the difference in modal-weighted temperatures is given by,

$$\begin{aligned} S_{\Delta T}(\omega) &= \mathcal{F}\{< [\overline{\delta T_1}(t) - \overline{\delta T_2}(t)][\overline{\delta T_1}(t+\tau) - \overline{\delta T_2}(t+\tau)] >\}(\omega) \\ &= S_{\overline{\delta T_1}}(\omega) + S_{\overline{\delta T_2}}(\omega) - 2Real\{\mathcal{F}[< \overline{\delta T_1}(t)\overline{\delta T_2}(t+\tau) >](\omega)\} \end{aligned} \tag{5.14}$$

where Fourier transformation is denoted by $\mathcal{F}$. With the definition,

$$R(\omega) = \frac{Real\{\mathcal{F}[< \overline{\delta T_1}(t)\overline{\delta T_2}(t+\tau) >](\omega)\}}{\sqrt{S_{\overline{\delta T_1}} S_{\overline{\delta T_2}}}}. \tag{5.15}$$

Eq. 5.14 gives Eq. 5.4 in the main text when the thermo-optic properties are taken into account.

In practice, the energy dissipation W_{diss} can be acquired by Fourier transformation of Eq. 5.7 with respect to t, yielding

$$i\omega\rho C\mathcal{F}\{\delta T\} - k\nabla^2\mathcal{F}\{\delta T\} = i\omega T_0 F_0 q(\mathbf{r}), \tag{5.16}$$

where $\omega = 2\pi f$ and only positive frequency components of δS are considered. An FEM solver (COMSOL multiphysics in this work) can be used for simulations using the above equation. Critical parameters used in the simulation of thermal properties are: density $\rho = 2.2 \times 10^3\ kg/m^3$, heat capacity $C = 740$ J/(kg·K), thermal conductivity $k = 1.38$ W/(m·K), thermorefractive index $n_T = 1.2 \times 10^{-5}$/K, and ambient temperature of 300 K. The silica resonator has 22 mm radius and 8 μm thickness, supported by a silicon pillar with 140 μm in undercut. The wedge angle is 30°.

Theory of noise transduction

In this section, we overview the theoretical analysis used to determine the noise transduction factors α and β. The following pair of Lugiato-Lefever equations [108, 112, 125] are utilized to predict the dynamics of the soliton field with another transverse mode family field coupled to it so as to provide dispersive wave radiation,

$$\frac{\partial E_{\mathrm{S}}}{\partial t} = (-\frac{\kappa_{\mathrm{S}}}{2} - i\delta\omega + i\frac{D_{2S}}{2}\frac{\partial^2}{\partial\phi^2} + ig_{\mathrm{S}}|E_{\mathrm{S}}|^2 + i\gamma_{\mathrm{S}}\frac{\partial|E_{\mathrm{S}}|^2}{\partial\phi})E_{\mathrm{S}} + f_o + iGE_{\mathrm{D}}, \tag{5.17}$$

$$\begin{aligned} \frac{\partial E_{\mathrm{D}}}{\partial t} = [&-\frac{\kappa_{\mathrm{D}}}{2} - i(\delta\omega + \Delta\omega_0 - i\Delta D\frac{\partial}{\partial\phi}) + i\frac{D_{2D}}{2}\frac{\partial^2}{\partial\phi^2} \\ &+ig_{\mathrm{D}}|E_{\mathrm{D}}|^2 + i\gamma_{\mathrm{D}}\frac{\partial|E_{\mathrm{D}}|^2}{\partial\phi}]E_{\mathrm{D}} + iGE_{\mathrm{S}}, \end{aligned} \tag{5.18}$$

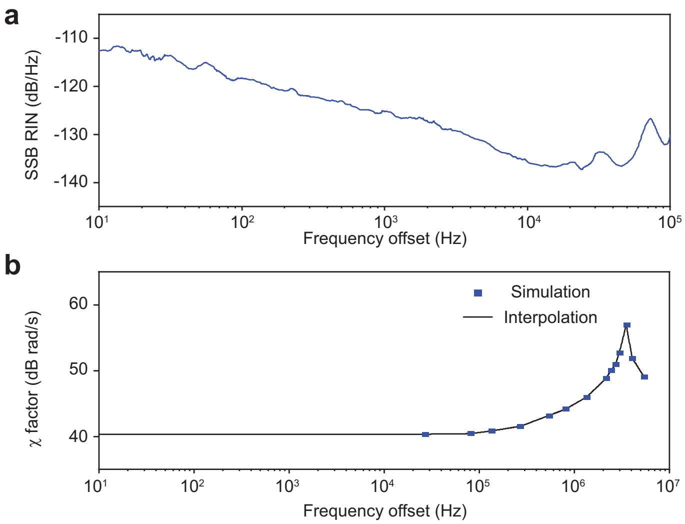

Figure 5.8: Influence of pump laser RIN. (a) Measured SSB RIN of the pump laser. (b) Simulated noise transduction factor $\chi(f)$ between pump laser RIN and soliton repetition rate.

where $E_{\rm S}$ ($E_{\rm D}$) is the slowly varying field envelope (photon number normalization) for the soliton (dispersive wave), $\kappa_{S,D}$ are the corresponding energy decay rates, $\delta\omega$ is the pump-cavity frequency detuning, $g_{\rm S,D} \equiv \hbar\omega_0^2 n_2 D_{\rm 1S,D}/2\pi n_0 A_{\rm eff}$ is the nonlinear coupling coefficient with $A_{\rm eff}$ the effective nonlinear mode area, $\gamma_{\rm S,D} \equiv g_{\rm S,D} D_{\rm 1S}\tau_R$ is the Raman coefficient with τ_R the Raman shock time, ϕ is azimuthal angle in the cavity, $\Delta\omega_0 \equiv \omega_{0D} - \omega_{0S}$, and $\Delta D \equiv D_{1D} - D_{1S}$. Also, $f_o \equiv \sqrt{\kappa_{\rm ext} P_{\rm in}}$ is the pump field amplitude where $\kappa_{\rm ext}$ is the external coupling rate of the soliton mode and $P_{\rm in}$ is the pump power. G is the coupling strength between the soliton and dispersive wave mode families.

After considerable algebra, the spectral recoil $\Omega_{\rm Recoil}$ induced by the dispersive wave can be obtained using moment analysis, as given by [108]

$$\Omega_{\rm Recoil} = -\Lambda\tau_{\rm s}|h_r|^2 \propto \frac{1}{(\Delta\omega')^2[(\Delta\omega_r - \Delta\omega')^2 + \frac{\kappa_{r-}^2}{4}]}, \tag{5.19}$$

with Λ

$$\Lambda = \frac{\pi r \kappa_{\rm D} g_{\rm S} D_{1S}^2}{\kappa_{\rm S} D_{2S}}. \tag{5.20}$$

Combined with the Raman-induced SSFS [98]

$$\Omega_{\rm Raman} = -\frac{8\tau_{\rm R} D_{\rm 2S}}{15\kappa_{\rm S} D_{1S}^2 \tau_{\rm s}^4}, \tag{5.21}$$

the overall soliton spectral shift yields

$$\Omega = \Omega_{\mathrm{Raman}} + \Omega_{\mathrm{Recoil}}. \tag{5.22}$$

In addition, the detuning $\delta\omega$ is obtained by [98, 108]

$$\delta\omega = \frac{D_{2S}}{2D_{1S}^2}(\frac{1}{\tau_{\mathrm{s}}^2} + \Omega^2). \tag{5.23}$$

It is noted Ω and τ_{s} are fitted through optical spectra of the soliton with a sech^2 envelope. All parameters that are required to describe the system are obtained either from direct measurement or by fitting experimental data. Critical parameters are: $\tau_{\mathrm{R}} = 2.7$ fs, $g_{\mathrm{S}} = 7.9 \times 10^{-4}$ rad/s. Fitted parameters include $G/2\pi = 11.55 \pm 2.03$ MHz and $\Delta\omega'/2\pi = 15.93 \pm 1.51$ MHz. Based on these parameters, the transduction factors are calculated numerically as shown in Fig. 5.5d. The analytical model is further verified with numerical simulation in the Supplement.

Impact of pump intensity noise

The impact of the relative intensity noise (RIN) from the pump laser on the soliton repetition rate is obtained by numerical simulation of the above-mentioned coupled Lugiato-Lefever equations. Specifically, a sinusoidal perturbation at frequency f is applied on the pump so that

$$f_o = f_s(1 + \frac{\varepsilon}{2}\sin 2\pi f t). \tag{5.24}$$

By tracking the motion of soliton peak position, the change of repetition rate can be revealed which further gives the following noise coupling coefficient:

$$\chi(f) = |\frac{\partial\omega_{\mathrm{rep}}}{\partial\epsilon}|. \tag{5.25}$$

Therefore, with the measured pump RIN (Fig. 5.8), the RIN-induced phase noise can be derived as shown in Fig. 5.3d.

Quantum timing jitter

Quantum timing jitter of soliton microcombs originates from vacuum fluctuations in each cavity mode. The predicted SSB phase noise spectral density of the detected soliton pulse stream at the repetition rate is given by [96]

$$S_{\mathrm{Q}}(f) = \frac{\pi g_{\mathrm{S}}}{6}\sqrt{\frac{2D_{2S}}{\delta\omega}}[\frac{\pi^2\kappa_{\mathrm{S}}}{16\delta\omega} + (1 + \frac{4\pi^2 f^2}{\kappa_{\mathrm{S}}^2})^{-1}\frac{\delta\omega}{\kappa_{\mathrm{S}}}]. \tag{5.26}$$

Chapter 6

ON-CHIP WEDGE MICRORESONATOR BRILLOUIN LASER REACHING THERMAL REFRACTIVE NOISE LIMIT

[5] Abstract

A on-chip thermal silica wedge microresonator Brillouin laser is demonstrated reaching thermal refractive noise limit by through suppression of Brillouin cascade. A fundamental frequency noise of 9×10^{-3} Hz^2/Hz is achieved. The results set new performance targets for chip-based Brillouin laser platforms.

Narrow-linewidth lasers are important to many applications including precision metrology, positioning, navigation, communications and sensing systems, and their chip-scale miniaturization is receiving increasing attention due to reduced size, smaller cost but comparable linewidth performance with bulk laser devices. Stimulated Brillouin lasers (SBLs) using high-Q optical microresonators have emerged as a powerful platform for narrow linewidth on-chip operation [10, 126]. SBLs have been demonstrated in many on-chip photonic platforms [24, 28, 32, 49, 127, 128]. On-chip SBL microlasers are key functional components for many powerful systems including Sagnac gyroscope [26, 28, 29], microwave synthesizer [30, 69] and microwave processor for communication [126].

Frequency noise is an important observable in laser systems. It is approximately described by two regime. Low offset regime (offset frequency 100 Hz - ~500 kHz) includes mainly the technical contribution to noise (such as noise coupled from the pump wave noise) and the fundamental source of noise (such as thermal refractive noise). High offset regime (offset frequency beyond ~500 kHz) is where white noise floor starts to manifest. This white noise floor is fundamental in nature and is critically important in applications that rely upon the beatnote of co-lasing waves such as Sagnac gyroscope and microwave generation where the technical noise and the thermal refractive noise are largely common mode and can be entirely cancelled, thus only fundamental noise contributions are left. As an example, ultra-

---

[5] Part of the work presented in this chapter has been published in "Towards milli-Hertz laser frequency noise on a chip," *CLEO* **SF2O.2**,(2021) [87]

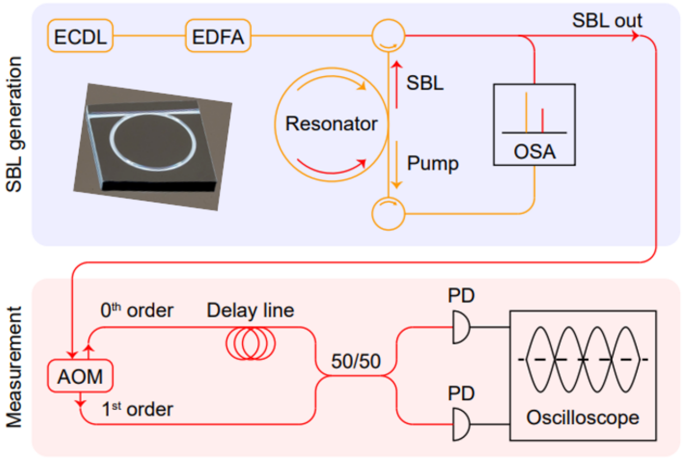

Figure 6.1: Experimental setup consisting of SBL generation and frequency noise measurement sections.

low fundamental noise enabled the extreme sensitivity to measure earth rotation using a single chip [29].

In this chapter, a frequency noise reaching thermal refractive noise limit and an ultra-low fundamental noise level of 9×10^{-3} $\mathrm{Hz}^2/\mathrm{Hz}$ in an on-chip SBL are demonstrated. The noise level has a power dependence and magnitude that are consistent with fundamental white frequency noise, and would correspond to a fundamental linewidth of 60 mHz. This linewidth is 5× lower than previous SBL reports, and it is measured using an enhanced self-heterodyne optical frequency discriminator method [129, 130]. The ultra-low noise level is made possible by the high optical Q of the resonator in combination with higher single-mode laser power through suppression of Brillouin cascade.

The interaction between acoustic waves and light waves generates Brillouin at a frequency down shifted position ($\Omega \sim 10.8$ GHz in silica) from the pump wave. The SBL occurs when a resonance mode sits in this Brillouin gain bandwidth ($\Gamma \sim 200$ MHz). The fast dissipation rates of Brillouin phonons (100 - 200 MHz) significantly suppresses the noise coupling from the pump light and enables generation of narrow-linewidth laser from a normal-linewidth laser. The fundamental noise formula for SBL exhibits Schawlow-Townes like behavior. It varies inversely with SBL optical power and roughly inverse-quadratically with cavity Q factor:

$$S_{\mathrm{SBL},F} = (1+\alpha^2)\frac{h\nu^3 n_{\mathrm{th}}}{2P_{\mathrm{SBL}}Q_{\mathrm{L}}Q_{\mathrm{ex}}} \tag{6.1}$$

These features provide effective ways to reduce fundamental noise of SBL: increase

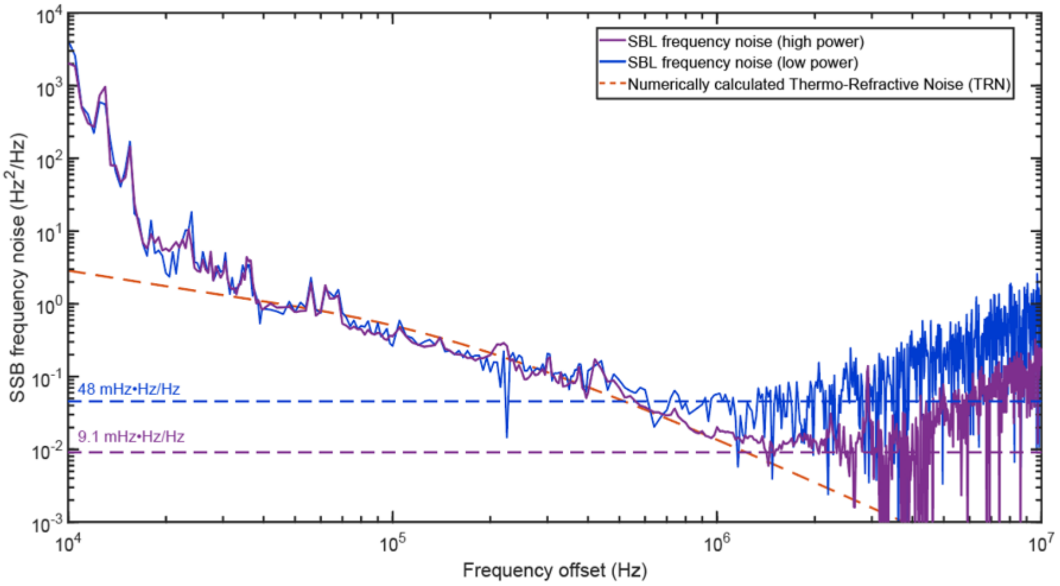

Figure 6.2: SBL single side-band frequency noise at two different power levels. The dashed red line gives the simulated thermo-refractive noise.

SBL output power and leverage ultra-high-Q microresonators [33].

Typically, to satisfy the phase matching condition, SBL microcavities are designed so as to align the free-spectral-range (FSR) to the Brillouin shift frequency. However, as the FSR dispersion is often small, a neighboring longitudinal mode can also phase match to the initial Stokes laser wave, leading to lasing cascade. Cascading is detrimental to low frequency noise operation as the laser power of the first Stokes wave (now the pumping wave) becomes clamped. Moreover, frequency noise is increased due to the presence of the second-order Stokes wave [131]. A natural strategy is to use different transverse mode families for pumping and Stokes waves to block cascade, so that Brillouin laser power can be substantially increased, resulting in reduced fundamental frequency noise.

A thermal silica wedge resonator is used for the SBL, which features FSR of 8.9 GHz, as shown in Fig. 6.1 inset. The resonator chip is optically packaged into a operational module [64]. Both pump mode and SBL mode feature high intrinsic Q-factors around 550 million (after packaging).

The experimental setup is shown in Fig. 6.1 An Pound-Drever-Hall locked external-cavity diode laser (ECDL) is amplified by an erbium-doped fiber amplifier (EDFA) and sent to a tapered fiber for coupling to the resonator. The Brillouin laser wave, propagating in the opposite direction of the pump wave, is collected with a circulator.

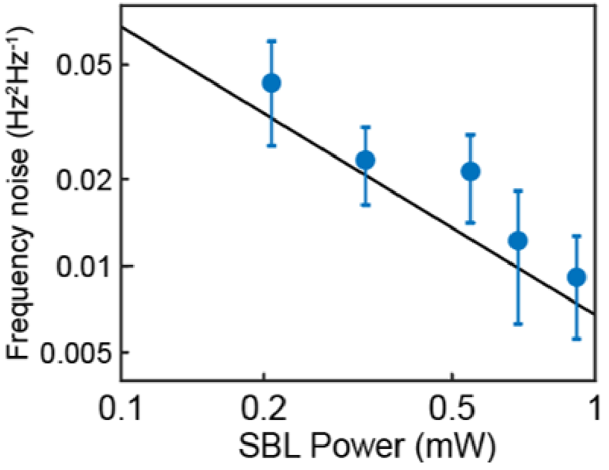

Figure 6.3: Dependence of SBL fundamental frequency noise levels on SBL output powers. Blue dots: data. Black solid line: theoretical prediction from Eq.6.1 $Q_L \approx 270$M, $Q_{ex} \approx 730$M). A good agreement is obtained.

An optical spectrum analyzer (OSA) is used to monitor pump and SBL spectra and to ensure that no cascading occurs.

To measure the frequency noise (more specifically, power spectral density), the laser output is sent to a self-heterodyne optical frequency discriminator enhanced with a cross correlation method (XCOR) [130]. The reason to implement cross correlation is that at high offset frequencies (above 1 MHz), the frequency noise floor and measurement sensitivity were found to be limited by technical noise from the photo-detectors (PD). The cross correlation of the electrical signals produced at the interferometer output is found effective to overcome this limitation. For operations, as shown in Fig. 6.1, an AOM was used to split the input light into frequency-shifted (1st order) and un-shifted parts (0th order), the latter being delayed by a 1-km-long fiber. However, instead of a single photodetector, two photodetectors receive the optical signals. Their outputs are recorded using an oscilloscope for subsequent XCOR to remove detector technical noise.

The SBL frequency noise measurement results are presented in Fig. 6.2 with a comparison of two SBL output powers. The purple solid line corresponds to 0.9 mW SBL output power and the blue solid line corresponds to 0.2 mW. Both traces overlap well at low offset frequencies (below 500 kHz) and they are limited by thermo-refractive noise (TRN) coming from dielectric resonator mode volume based on numerical simulation shown by red dashed line. The purple dashed line indicates the white noise floor at 0.9 mW. By averaging the white-like portion of

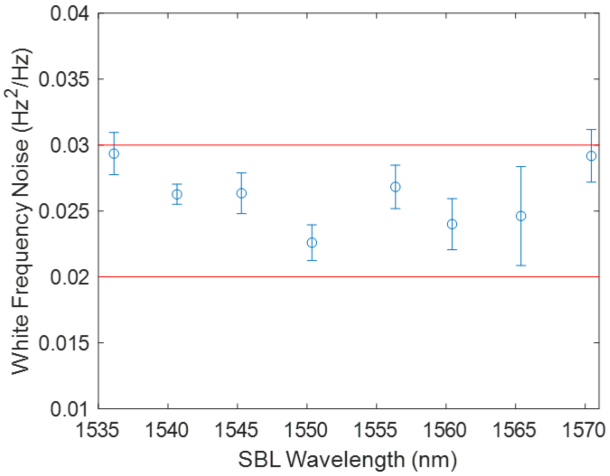

Figure 6.4: C/L band operations of ultra-low-fundamental noise SBL.

the measured frequency noise (between 1.5 MHz to 2 MHz), this noise floor is estimated to be 9×10^{-3} Hz^2/Hz (equivalent to a Lorentzian linewidth of 60 mHz). This is $1/5$ of the white noise floor at 0.2 mW (blue dashed line). The white noise floor at varied SBL output power levels is summarised in Fig. 6.3. And this noise is found to vary inversely with Stokes power and to also agree reasonably well with the theoretical predictions of the expected fundamental white noise level (see Eq.6.1 where $Q_\mathrm{L} \approx$ 270M and $Q_\mathrm{ex} \approx$ 730M are used), which proves its fundamental nature. The further increase of SBL output power is limited by the comb generation pumped by SBL in the anomalous dispersion region [132, 133]. This places a lower limit to the fundamental noise level:

$$S_{\mathrm{SBL},F} \geq (1+\alpha^2)\frac{h\nu^3 n_\mathrm{th}}{2Q_\mathrm{L}Q_\mathrm{ex}P_\mathrm{th}} = (1+\alpha^2)\frac{2h\nu^3 n_\mathrm{th} n_2 \eta^2}{n_\mathrm{g}^2 V_\mathrm{eff}} \tag{6.2}$$

where P_th is the parametric oscillation threshold [20, 58] and n_2 is the nonlinear refractive index ($n_{2\mathrm{silica}} = 2.2 \times 10^{-20}\mathrm{m}^2/\mathrm{W}$).

The wedge optical microresonators feature ultra-high-Q over very wide spectral band and high mode densities separated by hundreds of MHz in every FSR [33], which induces high probabilities of satisfying phase matching condition for SBL generation at any input wavelength, even into visible [56, 134]. As a demonstration, the ultra-low-fundamental noise SBL is measured over the whole C/L band (1535 nm - 1570 nm) as shown in Fig. 6.4. The fine tuning of SBL laser frequency in the GHz range can be achieved by either thermal tuning or piezo tuning through integrating these control elements with our photonic chips.

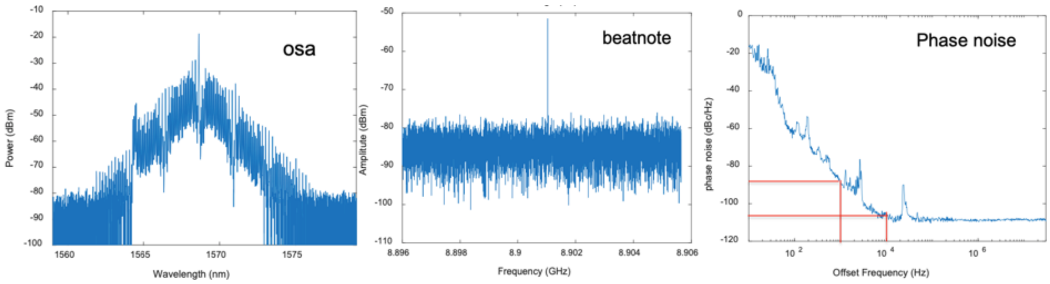

Figure 6.5: Multiple-soliton state generated by SBL. Optical spectrum, beatnote and 8.9 GHz microwave signal phase noise performance.

When the SBL output power reaches 1 mW ($\chi^{(3)}$ parametric oscillation threshold [33]), SBL starts to generate Kerr microcomb. And SBL pumped comb favors mode-locked soliton state [11]. One representative multiple-soliton state generated by SBL is presented in Fig. 6.5. The 8.9 GHz beatnote microwave signal features phase noise of -88 dBc/Hz at 1 kHz offset and -110 dBc/Hz at 10 kHz offset, a performance comparable with 'quiet point' operation result [88]. The reason is attributed to the low noise of SBL waves as soliton pump credited to the Brillouin acoustic filtering effect.

In summary, a 9×10^{-3} Hz^2/Hz ultra-low fundamental frequency noise in an on-chip SBL system at an output power of 0.9 mW has been demonstrated. This corresponds to 60 mHz fundamental Lorentzian linewidth. The boosted performance is enabled by a combination of ultra-high-Q factors with increased SBL power through suppression of Brillouin cascade by cross mode SBL operation. The same noise performance is measured over the whole C/L band. These results demonstrate the potential for silica-based high-Q laser platforms to achieve extremely narrow laser fundamental linewidths to a new target level . Even while the noise at low offset frequencies remains high, these noise sources can be suppressed in certain applications such as the Sagnac gyroscope that rely upon relative coherence of co-lasing waves [26].

Chapter 7

TM MODE ENABLES 700M INTEGRATED THIN SIN MICRORESONATORS

[6] Abstract

Recently, photonic integrated circuits based on high-aspect-ratio SiN waveguide structure is emerging as a powerful ultra-low-loss on-chip platform for applications spanning narrow-linewidth lasers to nonlinear optics. However, the Q-factors achieved are usually limited at the level of 200 million by scattering loss. In this chapter, by leveraging TM mode, Q factor as high as 680 million is achieved. The group velocity dispersion (GVD) of TM mode is 1/4 of TE mode. Both increased Q and reduced GVD are in favour of broad-bandwidth comb generation for applications such as optical frequency division (OFD).

Recently, photonic integrated circuits based on high-aspect-ratio SiN waveguide structure [13, 36, 135] is emerging as a powerful ultra-low-loss on-chip platform for applications spanning narrow-linewidth lasers to nonlinear optics. However, the Q-factors achieved are usually limited at the level of 200 million. The optical loss in high-aspect-ratio SiN waveguides is mainly limited by scattering loss at the SiN-silica interfaces. One natural strategy is to reduce the electric field strength at the interfaces. Compared with TE mode, TM mode feature much smaller field strength, with the trade off of larger mode area. In this chapter, by leveraging TM mode, Q factor as high as 680 million is achieved.

The theoretical analysis in the limit of infinite planar waveguides can show that the scattering loss ratio between TM and TE modes at the top/bottom core/cladding interfaces is:

$$\frac{\alpha_{\mathrm{TM0}}}{\alpha_{\mathrm{TE0}}} \approx \left(\frac{n_{\mathrm{cladding}}}{n_{\mathrm{core}}}\right)^6 \approx \frac{1}{7} \tag{7.1}$$

The infinite planar waveguide model is indeed a good approximation for the high-aspect-ratio SiN waveguide structure considering that the lateral dimension (~ 10 μm) are much larger than vertical dimension (100 nm).

---

[6] Work presented in this chapter has **not** been published yet.

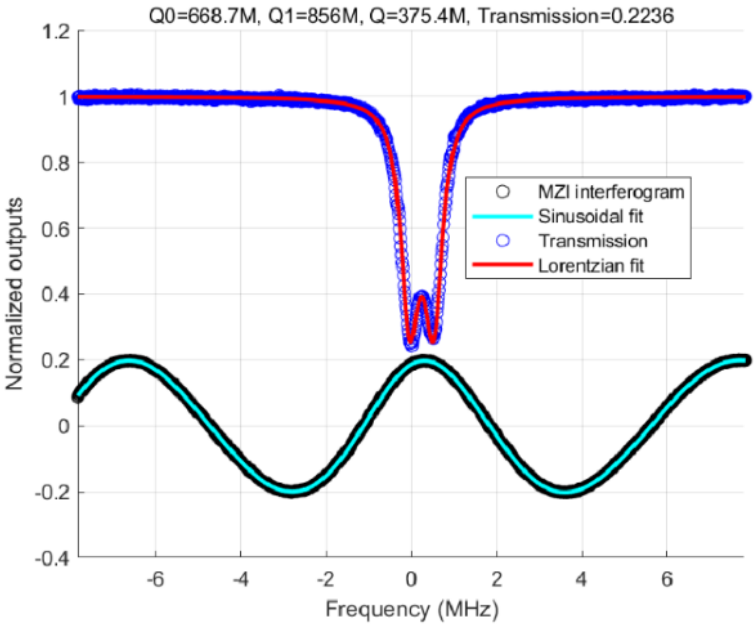

Figure 7.1: Resonance transmission linewidth measurement of a 8 GHz FSR device (8 mm diameter) at 1550 nm. Intrinsic Q-factor of Q_0 of 670 million and loaded Q-factor Q_L of 375 million are measured from fitting, with backscattering induced splitting of 0.56 MHz.

The device is fabricated in a CMOS foundry. The device is a microring with diameter of 8 mm, which corresponds to free-spectral-range (FSR) of 8 GHz. The core thin SiN thickness is 100 nm. The top cladding thickness is 4 μm and the under cladding thickness is 14.5 μm. Multiple factors specially for TM mode are carefully considered during the design process. First, ring waveguide width is increased to 20 μm to support 4 mm bending radius and only support single mode. Second, the device radius needs to be safely larger than cutoff bending radius and TM cutoff radius is much larger than TE. Last but the most importantly, the coupler is carefully designed. Because of the intrinsic loss rate (κ_i) of TM is much smaller than TE, the required coupling rate (κ_ex) to achieve critical coupling condition is much smaller. As a result, the gap between the bus waveguide and microring can be set very large to have very small coupling rate, while TE mode is super-undercoupled. As a side benefit of larger coupling gap, the intrinsic loss is further reduced because the perturbations of the coupling waveguide to the microresonator (usually perfectly symmetric) and this perturbation-induced scattering loss are reduced and higher Q is achieved. The coupling gap (edge to edge) is selected to be 9 μm and the coupling waveguide is selected to be 3.25 μm here.

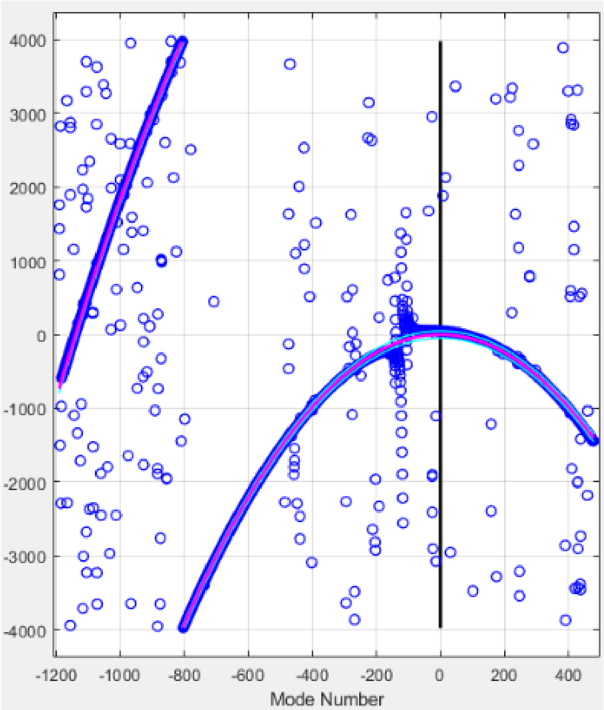

Figure 7.2: Resonance dispersion measurement. $D_2/2\pi$ of -12.3 kHz and FSR ($D_1/2\pi$) of 7.958 GHz are extracted . The crossing point at $\mu \approx -170$ results from TM/TE mode hybridization due to 0.5% difference in FSRs between TM and TE modes.

The device bus waveguide is interrogated through edge coupling using cleaved fiber with index match gel. TM mode feature large mode area, reduced mode ellipticity and better mode matching with fiber mode, so a 2 dB/facet edge loss is achieved assisted by chip edge waveguide tapering.

The Resonance transmission linewidth measurement result is shown in Fig. 7.1. From the fitting based on the split resonance model augmented with backscattering [85], the loaded Q-factor Q_{L} of 375 million, intrinsic Q-factor of Q_0 of 670 million and splitting of 0.56 MHz are extracted.

The microresonator (TM mode) dispersion measurement [121] is shown in Fig. 7.2. Based on the integrated dispersion relationship: $\omega_\mu = \omega_0 + D_1\mu + \frac{1}{2}D_2\mu^2$ (μ is the mode number relative to the reference center mode), $D_2/2\pi$ of -12.3 kHz and FSR ($D_1/2\pi$) of 7.958 GHz are obtained from data. Based on the relationship between waveguide group velocity dispersion (GVD) parameter (β_2) and resonator GVD parameter (D_2): $D_2 = -(c/n_g)\beta_2 D_1^2$, GVD β_2 of +154 ps^2/km is obtained. This number is one quarter of TE mode previously reported [13]. And reduced GVD is beneficial for increasing comb bandwidth, which is critically important for many applications such as optical frequency division (OFD) [136]. The bending radius of 4 mm induces the FSR difference between TM and TE modes. The FSR of TM mode is roughly 0.5% larger than that of TE mode, which causes the sing mode crossing point near 1560 nm ($\mu \approx -170$) from TM/TE mode hybridization. Such a mode crossing enables dark comb generation with normal dispersion only using continuous wave (CW) pump [137].

Chapter 8

ALGAAS SOLITON MICROCOMBS AT ROOM TEMPERATURE

[7] Abstract

Soliton mode locking in high-Q microcavities provides a way to integrate frequency comb systems. Among material platforms, AlGaAs has one of the largest optical nonlinearity coefficients, and is advantageous for low-pump-threshold comb generation. However, AlGaAs also has a very large thermo-optic effect that destabilizes soliton formation, and femtosecond soliton pulse generation has only been possible at cryogenic temperatures. Here, soliton generation in AlGaAs microresonators at room temperature is reported for the first time, to the best of our knowledge. The destabilizing thermo-optic effect is shown to instead provide stability in the high-repetition-rate soliton regime (corresponding to a large, normalized second-order dispersion parameter D_2/κ). Single soliton and soliton crystal generation with sub-milliwatt optical pump power are demonstrated. The generality of this approach is verified in a high-Q silica microtoroid where manual tuning into the soliton regime is demonstrated. Besides the advantages of large optical nonlinearity, these AlGaAs devices are natural candidates for integration with semiconductor pump lasers. Furthermore, the approach should generalize to any high-Q resonator material platform.

Optical frequency combs have revolutionized precision time and frequency metrology, and they find a wide range of applications in areas as diverse as spectroscopy, optical communications, distance measurement, and low-noise microwave generation [139]. Recent advances in chip-integration of optical frequency combs [11, 140–143] could accelerate their widespread use even beyond the laboratory environment. Taking advantage of chip-based high Q-factor microresonators [6], dissipative Kerr soliton (DKS) formation is a promising method of comb formation [11]. Because the Kerr nonlinearity exists in all optical materials, DKSs have been demonstrated in many materials including silicon nitride [105], silica [58] , aluminum nitride [144], and lithium niobate [117, 145].

---

[7] Work presented in this chapter has been published in "AlGaAs soliton microcombs at room temperature," *Optics Letters* **48**, 3853-3856 (2023) [138]

Among various materials, AlGaAs offers a combination of large nonlinearity and high refractive index that are well suited for low (μW-level) pump threshold [42, 43, 146, 147]. Moreover, because of its compatibility with semiconductor lasers, it has the potential to be integrated with pump lasers. However, the large thermo-optic effect of AlGaAs has prohibited femtosecond soliton pulse generation at room temperature, and either cooling to cryogenic temperature [120] or generation of dark soliton pulses [148] has been necessary to achieve stable microcombs. Here, we demonstrate stable room-temperature bright-soliton generation in AlGaAs microrosonators for the first time. Single soliton states are generated in waveguide-coupled AlGaAs microresonators at a repetition rate of 1 THz. The coherence of these soliton microcombs is confirmed by beatnote measurements with a self-referenced fiber comb system and observation of perfect soliton crystals (PSC) [149]. The approach uses the scaling of soliton power with the normalized second-order dispersion parameter D_2/κ [58], and is further verified by soliton generation in a high-Q silica microtoroid using only manual tuning (i.e., no special triggering [58]) of the optical pumping frequency.

Room temperature generation of solitons in AlGaAs is frustrated by a large thermo-optic coefficient with an abrupt drop of intra-cavity power that usually accompanies soliton formation [112]. The subsequent rapid cooling of the mode volume causes the resonator frequency to quickly tune away from the pumping frequency. If the thermo-optic effect is large, this tuning prevents stable soliton formation. On the other hand, the thermo-optic effect will also self-stabilize an optically pumped system if the intracavity power increases with laser blue-to-red tuning [150]. For soliton generation, the stability benefit of this increase has been noted in soliton crystal formation ([151, 152]).

To reduce the temperature decrease, a simple strategy is to increase soliton power. The emitted soliton power normalized by parametric oscillation threshold power is given by [58]:

$$\frac{P_{\mathrm{sol}}}{P_{\mathrm{th}}} = \frac{8\sqrt{2}\eta^2}{\pi}\sqrt{\frac{\delta\omega}{\kappa}}\sqrt{\frac{D_2}{\kappa}} \tag{8.1}$$

where $\delta\omega = \omega - \omega_0$ is the detuning of pumping frequency ω relative to the frequency ω_0 of the cavity mode that is pumped, D_2 is the second-order dispersion parameter (see Fig. 8.1b caption), and $\kappa = \omega/Q$ is the optical loss rate where Q is the optical Q-factor. Also, $\eta = Q/Q_{\mathrm{ex}}$ is the waveguide-to-resonator loading factor, where Q_{ex} is the external coupling Q factor ($1/Q = 1/Q_0 + 1/Q_{\mathrm{ex}}$ where Q_0 is the intrinsic Q factor). In Fig 8.1a, plots of Eq. 8.1 versus normalized detuning ($2\delta\omega/\kappa$) at several

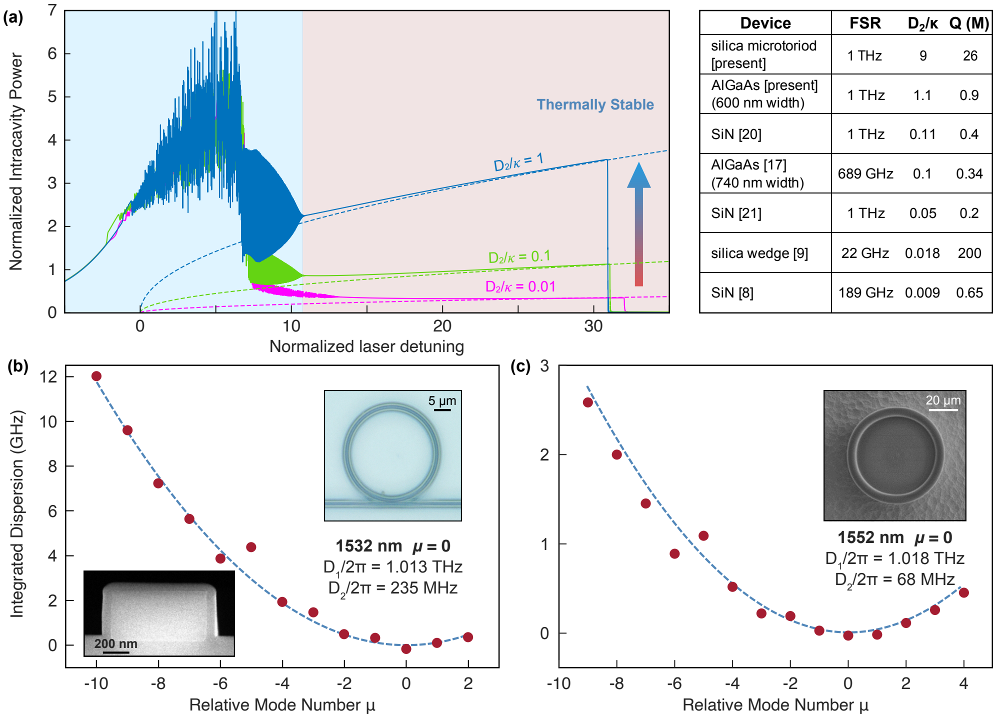

Device	FSR	D_2/κ	Q (M)
silica microtoroid [present]	1 THz	9	26
AlGaAs [present] (600 nm width)	1 THz	1.1	0.9
SiN [20]	1 THz	0.11	0.4
AlGaAs [17] (740 nm width)	689 GHz	0.1	0.34
SiN [21]	1 THz	0.05	0.2
silica wedge [9]	22 GHz	0.018	200
SiN [8]	189 GHz	0.009	0.65

Figure 8.1: AlGaAs and silica microresonator properties and soliton generation with increasing D_2/κ. (a) Numerical simulation of normalized intracavity power versus normalized pump laser detuning ($2\delta\omega/\kappa = 2(\omega - \omega_0)/\kappa$) for three microresonators having D_2/κ values of 1, 0.1, 0.01. The dashed lines are analytical results from Eq. 8.1. The pump power is set to 25 times parametric oscillation threshold for all three traces. Table summarizes D_2/κ values in various soliton generation devices from the references [58, 105, 118–120] and the devices tested in this work. (b) Measured integrated frequency dispersion for the AlGaAs resonator (red points) is plotted versus the relative mode number, μ. To construct this plot the center wavelength of each split mode is measured using an OSA. The mode frequency is given by $\omega_\mu = \omega_0 + \mu D_1 + \frac{1}{2}D_2\mu^2$ and the blue dashed curve is a fit using $D_1/2\pi$ = 1.0126 THz and $D_2/2\pi$ = 235 MHz. The measured modes span wavelengths from 1516 to 1620 nm and $\mu = 0$ corresponds to the pump mode wavelength at 1532 nm. A slight avoided mode crossing near $\mu = -5$ originates from TE/TM mode hybridization. Upper right inset: optical micrograph of the device with scale bar indicated. Lower left inset: SEM micrograph of AlGaAs waveguide cross section. (c) Silica microtoroid dispersion plot with the similar content to (b). Upper right inset: SEM micrograph of the device with scale bar indicated.

values of D_2/κ are superimposed on numerical simulations of normalized soliton power using the Lugiato Lefever equation [125]. Increasing D_2/κ results in higher soliton power at a given pump detuning. Since $D_2 = -(c/n_g)\beta_2 D_1^2$ (where β_2 is the group velocity dispersion, GVD), larger D_1 (equivalently larger FSR = $D_1/2\pi$ and

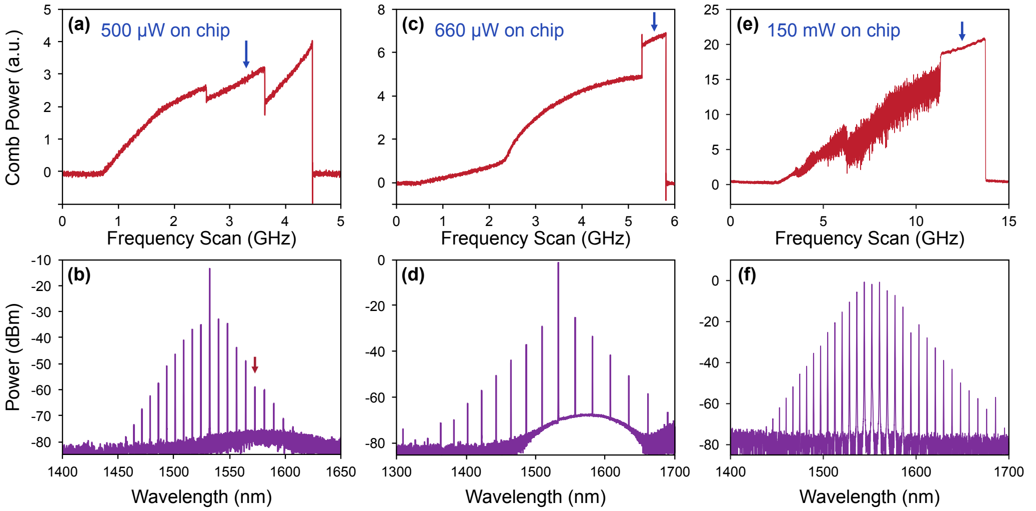

Figure 8.2: **AlGaAs microresonator and silica microtoroid soliton generation behavior at different pump power levels.** (a)-(b) Single soliton generation for 500 μW on-chip pump power showing soliton power versus pump frequency scan (a) and optical spectrum (b) at scan location given by the blue arrow in (a). (c)-(d) 3-FSR perfect soliton crystal formation at 660 μW on chip pump power with content similar to (a)-(b). (e)-(f) Scan (e) and optical spectrum (f) for soliton comb generation in the microtoroid resonator.

larger soliton repetition rate), larger β_2 and smaller κ will increase the normalized soliton power and mitigate the photothermal instability. A comparison of D_2/κ values taken from different devices reported in the literature as well as the devices studied here is provided in the Fig. 8.1a Table.

The $Al_{0.2}Ga_{0.8}As$ devices had FSR = 1 THz (12.46 μm radius) and details on their fabrication are provided in [43]. The microresonator waveguide cross section had 600 nm width and 400 nm height (see SEM image in Fig. 8.1b inset). With these dimensions, the fundamental TE mode has a calculated GVD β_2= -431 ps^2/km at 1532 nm (the pumping wavelength in this study). This value is in good agreement with the measured microresonator GVD $\beta_2 = -n_g D_2/cD_1^2 \approx -455$ ps^2/km (see Fig. 8.1b and caption for dispersion measurement details). Intrinsic Q factor $Q_0 = 1.7$ million and total Q factor $Q = 0.92$ M at the pumping wavelength were measured by characterizing the transmission spectrum. The spectrum featured a full-width-half-maximum linewidth of $\kappa/2\pi = 210$ MHz which was broadened slightly by mode-splitting of 92 MHz [85]. The parametric oscillation threshold was measured (in-waveguide) to be approximately 20 μW which is in good agreement with the theoretical value of 22 μW [20, 58] where $n_2 \approx 1.7\times10^{-17}$ m^2/W [55] was assumed in addition to the following calculated parameters: effective index n_{eff}=2.899, group index n_g=3.746, and effective mode area A_{eff}= 0.256 μm^2). The refractive index of $Al_{0.2}Ga_{0.8}As$ is taken from the material refractive index database [153].

The high-Q silica microtoroid used in this work was fabricated by laser reflow and optical coupling employed a tapered fiber as descibed elsewhere [20]. It featured an FSR of 1.018 THz (see SEM image in the inset of Fig. 8.1c). Intrinsic Q factor Q_0 = 37 million and total Q factor Q = 26 million were measured.

Both AlGaAs and silica microcomb devices were pumped using a tunable ECDL (Toptica CTL1550). For AlGaAs measurements the laser light was coupled in/out of the chip bus waveguide through a pair of fiber lenses and pump power is adjusted by a variable optical attenuator and monitored before and after the resonator chip by integrating sphere power meters (ISPMs). The ISPMs allowed estimate of the coupling loss to the chip to be 3.3 dB per facet. The bus waveguides were tapered to 200 nm to minimize this loss. Silica microtoroid devices were pumped using a fiber taper with less than 0.5 dB insertion loss.

A summary of AlGaAs microcomb behavior for pumping at 1532 nm is provided in Fig. 8.2 a-d. Beginning with panels Fig. 8.2 a-b, panel a gives the comb power for constant on-chip bus waveguide pump power of 500 μW as the pump laser is scanned in frequency (horizontal axis). A Mach-Zehnder interferometer is used to calibrate the laser frequency scan. The pump line is filtered using a WaveShaper. As can be seen in Fig. 8.2a, the power initially decreases slightly where the system transitions to a single soliton state. However, the soliton power eventually rises above the initial power drop and the photothermal effect works to stabilize the system. In fact, it was possible to manually tune the laser frequency into the soliton state and stably measure comb spectra as has been reported elsewhere [118, 119]. A single soliton spectrum measured at the detuning indicated by the blue arrow in Fig. 8.2a is presented in Fig. 8.2b. The comb line spacing equals one FSR (1 THz, 8 nm). As an aside, the 1572 nm comb line (indicated by the red arrow) is reduced in power as a result of the perturbation to the parabolic dispersion at $\mu = -5$ in Fig. 8.1b. Also, the state appearing in Fig. 8.2a for larger detuning than the single soliton state is believed to result from mode-locking on a hybrid mode state associated with the mode spliting. This state is under further investigation.

In Figs. 8.2c-d, the same measurements are repeated for 660 μW on chip pumping power. Here, the optical spectrum in Fig. 8.2d reveals that the state is a perfect soliton crystal state [149, 151] with its repetition rate equal to 3 FSRs (3 THz,

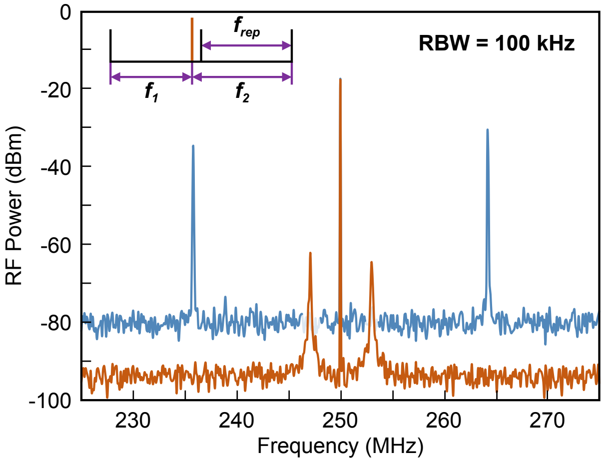

Figure 8.3: **Single soliton comb line beatnote with self-referenced fiber comb.** The peak at 250 MHz gives the fiber comb repetition rate f_{rep}. In the red trace, the 2 small peaks are beatnotes between the filtered 1548 nm single soliton comb line with 2 fiber comb lines (see inset). The blue trace is the beatnote of the ECDL laser pump line with two fiber comb lines.

24 nm), corresponding to three soliton pulses circulating in the cavity. The comb spectrum is spectrally broad spanning 400 nm (1300-1700 nm). Importantly, the ability to observe a soliton crystal further confirms the coherence of the soliton pulses in this system, since this is required to form the 3 FSR comb from coherent interference of three underlying 1 FSR combs.

Finally, Figs. 8.2e-f show soliton power versus tuning and single soliton comb spectra for the microtoroid device. Significantly, on account of the large D_2/κ for this device (see Table in Fig. 8.1a) the soliton step rises. As a result, it was possible to excite this soliton using only manual tuning. As an aside, the large D_2/κ value of these systems also means that parametric oscillation initiates on the neighboring sidemodes of the pumping mode. Specifically, the peak parametric gain occurs at $\mu - \mu_{\text{pump}} \approx \sqrt{\kappa/D_2} \approx 1$ [11].

To further confirm microcomb formation in the single soliton state of the AlGaAs device, one of the comb lines (1548 nm line in Fig. 8.2b, $\mu = -2$) is filtered out and beat with a self-referenced [3] fiber comb (Menlo FC1500-250-ULN, f_{rep}=250 MHz and carrier-envelope-offset frequency $f_{\text{CEO}} = 35$ MHz). The beatnote between microcomb and fiber comb is shown in Fig. 8.3 as the red trace. The strong peak is the fiber comb repetition rate, while the neighboring weaker peaks are beatnotes produced by two fiber comb teeth with the filtered THz comb tooth. The beatnote peak at 247.1 MHz has a full width at half maximum linewidth of 59 kHz, which is an order-of-magnitude narrower than in previous work at 4K temperature [120]. For comparison, the beatnote between the pump laser (Toptica ECDL) and the fiber comb is also plotted as the blue trace. As an aside, on account of the THz repetition rate, it was not possible to directly detect the comb rate [154]. Likewise, autocorrelation measurements were difficult due to the sub femto Joule pulse energy. Also, amplification of the pulses was challenging due to the limited bandwidth of erbium fiber amplifiers in comparison to the soliton spectrum.

We have demonstrated soliton generation in AlGaAs microresonators at room temperature for the first time. In the experiment, large D_2/κ resonators were used to create higher power soliton steps and leverage the large thermo-optical effect to stabilize (as opposed to destabilize) soliton formation. Low-noise 1 THz repetition-rate soliton generation was possible with only sub-milliWatt optical pump power. Combined with on-chip optical amplifiers [155], such a high repetition-rate optical pulse source can be useful in applications such as pulse driven optical computation [156, 157] (e.g. coherent Ising machine [158, 159]) and for THz wave generation [154]. It should also be possible to integrate these devices with III-V pump lasers, e.g., by further using heterogeneous integration of InP laser on top of nonlinear waveguides [160]. Finally, the same strategy of increasing D_2/κ should be applicable for soliton generation in all material systems, including other semiconductor systems such as GaP [46]. To demonstrate the generality of this approach, soliton generation in high-Q silica microtoroids was demonstrated using only manual tuning of the pumping frequency to initiate soliton formation.

BIBLIOGRAPHY

1. Maiman, T. H. "Stimulated Optical Radiation in Ruby". *Nature* **187,** 493–494 (1960).
2. Schawlow, A. L. & Townes, C. H. "Infrared and Optical Masers". *Phys. Rev.* **112,** 1940–1949 (1958).
3. Jones, D. J. *et al.* "Carrier-envelope phase control of femtosecond mode-locked lasers and direct optical frequency synthesis". *Science* **288,** 635–639 (2000).
4. Li, T. "Optical Fiber Communications: Fiber Fabrication" (Academic Press, 1985).
5. Keiser, G. "Optical fiber communications (4th edition)" (McGraw-Hill Education, 2010).
6. Vahala, K. J. "Optical microcavities". *Nature* **424,** 839–846 (2003).
7. Del'Haye, P. *et al.* "Optical frequency comb generation from a monolithic microresonator". *Nature* **450,** 1214–1217 (2007).
8. Kippenberg, T. J., Holzwarth, R. & Diddams, S. A. "Microresonator-Based Optical Frequency Combs". *Science* **332,** 555–559 (2011).
9. Pasquazi, A. *et al.* "Micro-combs: A novel generation of optical sources". *Physics Reports* **729,** 1–81 (2018).
10. Li, J., Lee, H., Chen, T. & Vahala, K. J. "Characterization of a high coherence, Brillouin microcavity laser on silicon". *Opt. Express* **20,** 20170–20180 (2012).
11. Kippenberg, T. J., Gaeta, A. L., Lipson, M. & Gorodetsky, M. L. "Dissipative Kerr solitons in optical microresonators". *Science* **361,** eaan8083 (2018).
12. Lee, H. *et al.* "Spiral resonators for on-chip laser frequency stabilization". *Nature Communications* **4,** 2468 (2013).
13. Jin, W. *et al.* "Hertz-linewidth semiconductor lasers using CMOS-ready ultra-high-Q microresonators". *Nature Photonics* **15,** 346–353 (2021).
14. Eichenfield, M., Chan, J., Camacho, R. M., Vahala, K. J. & Painter, O. "Optomechanical crystals". *Nature* **462,** 78–82 (2009).
15. Kippenberg, T. J. & Vahala, K. J. "Cavity Optomechanics: Back-Action at the Mesoscale". *Science* **321,** 1172–1176 (2008).
16. Xu, Q., Schmidt, B., Pradhan, S. & Lipson, M. "Micrometre-scale silicon electro-optic modulator". *Nature* **435,** 325–327 (2005).

17. Spencer, D. T. *et al.* "An optical-frequency synthesizer using integrated photonics". *Nature* **557,** 81–85 (2018).

18. Newman, Z. L. *et al.* "Architecture for the photonic integration of an optical atomic clock". *Optica* **6,** 680–685 (2019).

19. Spillane, S. M., Kippenberg, T. J. & Vahala, K. J. "Ultralow-threshold Raman laser using a spherical dielectric microcavity". *Nature* **415,** 621–623 (2002).

20. Kippenberg, T. J., Spillane, S. M. & Vahala, K. J. "Kerr-Nonlinearity Optical Parametric Oscillation in an Ultrahigh-Q Toroid Microcavity". *Phys. Rev. Lett.* **93,** 083904 (2004).

21. Savchenkov, A. A. *et al.* "Low Threshold Optical Oscillations in a Whispering Gallery Mode CaF_2 Resonator". *Phys. Rev. Lett.* **93,** 243905 (2004).

22. Tomes, M. & Carmon, T. "Photonic Micro-Electromechanical Systems Vibrating at X-band (11-GHz) Rates". *Phys. Rev. Lett.* **102,** 113601 (2009).

23. Grudinin, I. S., Matsko, A. B. & Maleki, L. "Brillouin Lasing with a CaF_2 Whispering Gallery Mode Resonator". *Phys. Rev. Lett.* **102,** 043902 (2009).

24. Lee, H. *et al.* "Chemically etched ultrahigh-Q wedge-resonator on a silicon chip". *Nature Photonics* **6,** 369–373 (2012).

25. Li, B. *et al.* "Reaching fiber-laser coherence in integrated photonics". *Opt. Lett.* **46,** 5201–5204 (2021).

26. Li, J., Suh, M.-G. & Vahala, K. "Microresonator Brillouin gyroscope". *Optica* **4,** 346–348 (2017).

27. Liang, W. *et al.* "Resonant microphotonic gyroscope". *Optica* **4,** 114–117 (2017).

28. Gundavarapu, S. *et al.* "Sub-Hertz fundamental linewidth photonic integrated Brillouin laser". *Nature Photonics* **13,** 60–67 (2019).

29. Lai, Y.-H. *et al.* "Earth rotation measured by a chip-scale ring laser gyroscope". *Nature Photonics* **14,** 345–349 (2020).

30. Li, J., Lee, H. & Vahala, K. J. "Microwave synthesizer using an on-chip Brillouin oscillator". *Nature Communications* **4,** 2097 (2013).

31. Liang, W. *et al.* "High spectral purity Kerr frequency comb radio frequency photonic oscillator". *Nature Communications* **6,** 7957 (2015).

32. Yang, K. Y. *et al.* "Bridging ultrahigh-Q devices and photonic circuits". *Nature Photonics* **12,** 297–302 (2018).

33. Wu, L., Wang*, H., Yang, Q.-F., Ji, Q.-X., Shen, B., Bao, C., Gao, M. & Vahala, K. "Greater than one billion Q factor for on-chip microresonators". *Opt. Lett.* **45,** 5129–5131. `http://dx.doi.org/10.1364/OL.394940` (2020).

34. Armani, D. K., Kippenberg, T. J., Spillane, S. M. & Vahala, K. J. "Ultra-high-Q toroid microcavity on a chip". *Nature* **421,** 925–928 (2003).

35. Moss, D. J., Morandotti, R., Gaeta, A. L. & Lipson, M. "New CMOS-compatible platforms based on silicon nitride and Hydex for nonlinear optics". *Nature Photonics* **7,** 597–607 (2013).

36. Puckett, M. W. *et al.* "422 Million intrinsic quality factor planar integrated all-waveguide resonator with sub-MHz linewidth". *Nature Communications* **12,** 934 (2021).

37. Liu, K. *et al.* "Ultralow 0.034 dB/m loss wafer-scale integrated photonics realizing 720 million Q and 380 μW threshold Brillouin lasing". *Optics Letters* **47,** 1855–1858 (2022).

38. Liu, J. *et al.* "High-yield, wafer-scale fabrication of ultralow-loss, dispersion-engineered silicon nitride photonic circuits". *Nature Communications* **12,** 2236 (2021).

39. Ji, X. *et al.* "Ultra-low-loss on-chip resonators with sub-milliwatt parametric oscillation threshold". *Optica* **4,** 619–624 (2017).

40. Bogaerts, W. *et al.* "Silicon microring resonators". *Laser & Photonics Reviews* **6,** 47–73 (2012).

41. Zhang, M., Wang, C., Cheng, R., Shams-Ansari, A. & Lončar, M. "Monolithic ultra-high-Q lithium niobate microring resonator". *Optica* **4,** 1536–1537 (2017).

42. Chang, L. *et al.* "Ultra-efficient frequency comb generation in AlGaAs-on-insulator microresonators". *Nature Communications* **11,** 1331 (2020).

43. Xie, W. *et al.* "Ultrahigh-Q AlGaAs-on-insulator microresonators for integrated nonlinear photonics". *Opt. Express* **28,** 32894–32906 (2020).

44. Jung, H. *et al.* "Tantala Kerr nonlinear integrated photonics". *Optica* **8,** 811–817 (2021).

45. Gong, Z. *et al.* "High-fidelity cavity soliton generation in crystalline AlN micro-ring resonators". *Opt. Lett.* **43,** 4366–4369 (2018).

46. Wilson, D. J. *et al.* "Integrated gallium phosphide nonlinear photonics". *Nature Photonics* **14,** 57–62 (2020).

47. Hausmann, B. J. M., Bulu, I., Venkataraman, V., Deotare, P. & Lončar, M. "Diamond nonlinear photonics". *Nature Photonics* **8,** 369–374 (2014).

48. Lukin, D. M. *et al.* "4H-silicon-carbide-on-insulator for integrated quantum and nonlinear photonics". *Nature Photonics* **14,** 330–334 (2020).

49. Kim, D.-G. *et al.* "Universal light-guiding geometry for on-chip resonators having extremely high Q-factor". *Nature Communications* **11,** 5933 (2020).

50. Schilling, R. *et al.* "Ultrahigh-Q on-chip silicon–germanium microresonators". *Optica* **9,** 284–287 (2022).

51. Gorodetsky, M. L., Savchenkov, A. A. & Ilchenko, V. S. "Ultimate Q of optical microsphere resonators". *Opt. Lett.* **21,** 453–455 (1996).

52. Grudinin, I. S., Ilchenko, V. S. & Maleki, L. "Ultrahigh optical Q factors of crystalline resonators in the linear regime". *Phys. Rev. A* **74,** 063806 (2006).

53. Del'Haye, P., Diddams, S. A. & Papp, S. B. "Laser-machined ultra-high-Q microrod resonators for nonlinear optics". *Appl. Phys. Lett.* **102,** 221119 (2013).

54. Savchenkov, A. A., Ilchenko, V. S., Matsko, A. B. & Maleki, L. "Kilohertz optical resonances in dielectric crystal cavities". *Phys. Rev. A* **70,** 051804 (2004).

55. Gao, M. *et al.* "Probing material absorption and optical nonlinearity of integrated photonic materials". *Nature Communications* **13,** 3323 (2022).

56. Wu, L., Gao, M., Liu, J.-Y., Chen, H.-J., Colburn, K., Blauvelt, H. A. & Vahala, K. J. "Hydroxyl ion absorption in on-chip high-Q resonators". *Opt. Lett.* **48,** 3511–3514. `http://dx.doi.org/10.1364/OL.492067` (2023).

57. Yariv, A. "Universal relations for coupling of optical power between microresonators and dielectric waveguides". *Electronics Letters* **36,** 321–322 (2000).

58. Yi, X., Yang, Q.-F., Yang, K. Y., Suh, M.-G. & Vahala, K. "Soliton frequency comb at microwave rates in a high-Q silica microresonator". *Optica* **2,** 1078–1085 (2015).

59. Sun, C. *et al.* "Single-chip microprocessor that communicates directly using light". *Nature* **528,** 534–538 (2015).

60. Lee, B. G., Nedovic, N., Greer, T. H. & Gray, C. T. "Beyond CPO: A Motivation and Approach for Bringing Optics Onto the Silicon Interposer". *Journal of Lightwave Technology* **41,** 1152–1162 (2023).

61. Cai, M., Painter, O. & Vahala, K. J. "Observation of Critical Coupling in a Fiber Taper to a Silica-Microsphere Whispering-Gallery Mode System". *Phys. Rev. Lett.* **85,** 74–77 (2000).

62. Spillane, S. M., Kippenberg, T. J., Painter, O. J. & Vahala, K. J. "Ideality in a Fiber-Taper-Coupled Microresonator System for Application to Cavity Quantum Electrodynamics". *Phys. Rev. Lett.* **91,** 043902 (2003).

63. Lai, Y.-H., Yang, K. Y., Suh, M.-G. & Vahala, K. J. "Fiber taper characterization by optical backscattering reflectometry". *Opt. Express* **25,** 22312–22327 (2017).

64. Suh, M.-G., Wang, C. Y., Johnson, C. & Vahala, K. J. "Directly pumped 10GHz microcomb modules from low-power diode lasers". *Opt. Lett.* **44,** 1841–1843 (2019).

65. Suh, M.-G., Yang, Q.-F., Yang, K. Y., Yi, X. & Vahala, K. J. "Microresonator soliton dual-comb spectroscopy". *Science* **354,** 600–603 (2016).

66. Yang, Q.-F. *et al.* "Vernier spectrometer using counterpropagating soliton microcombs". *Science* **363,** 965–968 (2019).

67. Suh, M.-G. & Vahala, K. J. "Soliton microcomb range measurement". *Science* **359,** 884–887 (2018).

68. Bao, C., Suh, M.-G. & Vahala, K. "Microresonator soliton dual-comb imaging". *Optica* **6,** 1110–1116 (2019).

69. Li, J., Yi, X., Lee, H., Diddams, S. A. & Vahala, K. J. "Electro-optical frequency division and stable microwave synthesis". *Science* **345,** 309–313 (2014).

70. Lee, H., Chen, T., Li, J., Painter, O. & Vahala, K. J. "Ultra-low-loss optical delay line on a silicon chip". *Nature Communications* **3,** 867 (2012).

71. Chen, T., Lee, H. & Vahala, K. J. "Thermal stress in silica-on-silicon disk resonators". *Appl. Phys. Lett.* **102,** 031113 (2013).

72. Suh, M.-G. & Vahala, K. "Gigahertz-repetition-rate soliton microcombs". *Optica* **5,** 65–66 (2018).

73. Carmon, T., Yang, L. & Vahala, K. J. "Dynamical thermal behavior and thermal self-stability of microcavities". *Opt. Express* **12,** 4742–4750 (2004).

74. Spencer, D. T., Bauters, J. F., Heck, M. J. R. & Bowers, J. E. "Integrated waveguide coupled Si3N4 resonators in the ultrahigh-Q regime". *Optica* **1,** 153–157 (2014).

75. Humbach, O., Fabian, H., Grzesik, U., Haken, U. & Heitmann, W. "Analysis of OH absorption bands in synthetic silica". *Journal of Non-Crystalline Solids* **203,** 19–26 (1996).

76. Barwicz, T. & Haus, H. A. "Three-Dimensional Analysis of Scattering Losses Due to Sidewall Roughness in Microphotonic Waveguides". *J. Lightwave Technol.* **23,** 2719–2732 (2005).

77. Olshansky, R. "Propagation in glass optical waveguides". *Rev. Mod. Phys.* **51,** 341–367 (1979).

78. Thomas, G. A., Shraiman, B. I., Glodis, P. F. & Stephen, M. J. "Towards the clarity limit in optical fibre". *Nature* **404,** 262–264 (2000).

79. Wilson, R. G. "Secondary Ion Mass Spectrometry : a practical handbook for depth profiling and bulk impurity analysis" (Wiley, 1989).

80. Hauri, E. *et al.* “SIMS analysis of volatiles in silicate glasses: 1. Calibration, matrix effects and comparisons with FTIR”. *Chemical Geology* **183,** 99–114 (2002).

81. Mosenfelder, J. L. *et al.* “Analysis of hydrogen in olivine by SIMS: Evaluation of standards and protocol”. *American Mineralogist* **96,** 1725–1741 (2011).

82. Rokhsari, H., Spillane, S. M. & Vahala, K. J. “Loss characterization in microcavities using the thermal bistability effect”. *Appl. Phys. Lett.* **85,** 3029–3031 (2004).

83. Honari, S., Haque, S. & Lu, T. “Fabrication of ultra-high Q silica microdisk using chemo-mechanical polishing”. *Appl. Phys. Lett.* **119,** 031107 (2021).

84. Gorodetsky, M. L., Pryamikov, A. D. & Ilchenko, V. S. “Rayleigh scattering in high-Q microspheres”. *J. Opt. Soc. Am. B* **17,** 1051–1057 (2000).

85. Kippenberg, T. J., Spillane, S. M. & Vahala, K. J. “Modal coupling in traveling-wave resonators”. *Opt. Lett.* **27,** 1669–1671 (2002).

86. Ghulinyan, M., Bernard, M., Bartali, R. & Pucker, G. “Formation of Mach angle profiles during wet etching of silica and silicon nitride materials”. *Applied Surface Science* **359,** 679–686 (2015).

87. Wang*, H., Wu*, L., Yuan*, Z. & Vahala, K. “Towards milli-Hertz laser frequency noise on a chip”. in *CLEO* (2021), SF2O.2. `http://dx.doi.org/10.1364/CLEO_SI.2021.SF2O.2`.

88. Yang*, Q.-F., Ji*, Q.-X., Wu*, L., Shen, B., Wang, H., Bao, C., Yuan, Z. & Vahala, K. “Dispersive-wave induced noise limits in miniature soliton microwave sources”. *Nature Communications* **12,** 1442. `https://doi.org/10.1038/s41467-021-21658-7` (2021).

89. Bernard, M. *et al.* “Top-down convergence of near-infrared photonics with silicon substrate-integrated electronics”. *Optica* **8,** 1363–1364 (2021).

90. Xiang, C. *et al.* “3D integration enables ultralow-noise isolator-free lasers in silicon photonics”. *Nature* **620,** 78–85 (2023).

91. Herr, T. *et al.* “Mode Spectrum and Temporal Soliton Formation in Optical Microresonators”. *Phys. Rev. Lett.* **113,** 123901 (2014).

92. Liu, J. *et al.* “Photonic microwave generation in the X- and K-band using integrated soliton microcombs”. *Nature Photonics* **14,** 486–491 (2020).

93. Shen, B. *et al.* “Integrated turnkey soliton microcombs”. *Nature* **582,** 365–369 (2020).

94. Tang, J. *et al.* “Integrated optoelectronic oscillator”. *Opt. Express* **26,** 12257–12265 (2018).

95. Do, P. T. *et al.* “Wideband tunable microwave signal generation in a silicon-micro-ring-based optoelectronic oscillator”. *Scientific Reports* **10,** 6982 (2020).

96. Matsko, A. B. & Maleki, L. "On timing jitter of mode locked Kerr frequency combs". *Opt. Express* **21,** 28862–28876 (2013).
97. Bao, C. *et al.* "Quantum diffusion of microcavity solitons". *Nature Physics* **17,** 462–466 (2021).
98. Yi, X., Yang, Q.-F., Yang, K. Y. & Vahala, K. "Theory and measurement of the soliton self-frequency shift and efficiency in optical microcavities". *Opt. Lett.* **41,** 3419–3422 (2016).
99. Karpov, M. *et al.* "Raman Self-Frequency Shift of Dissipative Kerr Solitons in an Optical Microresonator". *Phys. Rev. Lett.* **116,** 103902 (2016).
100. Yang, Q.-F., Yi, X., Yang, K. Y. & Vahala, K. "Spatial-mode-interaction-induced dispersive waves and their active tuning in microresonators". *Optica* **3,** 1132–1135 (2016).
101. Gorodetsky, M. L. & Grudinin, I. S. "Fundamental thermal fluctuations in microspheres". *J. Opt. Soc. Am. B* **21,** 697–705 (2004).
102. Matsko, A. B., Savchenkov, A. A., Yu, N. & Maleki, L. "Whispering-gallery-mode resonators as frequency references. I. Fundamental limitations". *J. Opt. Soc. Am. B* **24,** 1324–1335 (2007).
103. Kondratiev, N. & Gorodetsky, M. "Thermorefractive noise in whispering gallery mode microresonators: Analytical results and numerical simulation". *Physics Letters A* **382,** 2265–2268 (2018).
104. Huang, G. *et al.* "Thermorefractive noise in silicon-nitride microresonators". *Phys. Rev. A* **99,** 061801 (2019).
105. Brasch, V. *et al.* "Photonic chip–based optical frequency comb using soliton Cherenkov radiation". *Science* **351,** 357–360 (2016).
106. Jang, J. K., Erkintalo, M., Murdoch, S. G. & Coen, S. "Observation of dispersive wave emission by temporal cavity solitons". *Opt. Lett.* **39,** 5503–5506 (2014).
107. Nielsen, A. U., Garbin, B., Coen, S., Murdoch, S. G. & Erkintalo, M. "Emission of intense resonant radiation by dispersion-managed Kerr cavity solitons". *APL Photonics* **3,** 120804 (2018).
108. Yi, X. *et al.* "Single-mode dispersive waves and soliton microcomb dynamics". *Nature Communications* **8,** 14869 (2017).
109. Yi, X., Yang, Q.-F., Yang, K. Y. & Vahala, K. "Active capture and stabilization of temporal solitons in microresonators". *Opt. Lett.* **41,** 2037–2040 (2016).
110. Guo, H. *et al.* "Intermode Breather Solitons in Optical Microresonators". *Phys. Rev. X* **7,** 041055 (2017).

111. Lucas, E., Guo, H., Jost, J. D., Karpov, M. & Kippenberg, T. J. "Detuning-dependent properties and dispersion-induced instabilities of temporal dissipative Kerr solitons in optical microresonators". *Phys. Rev. A* **95,** 043822 (2017).

112. Herr, T. *et al.* "Temporal solitons in optical microresonators". *Nature Photonics* **8,** 145–152 (2014).

113. Stone, J. R. *et al.* "Thermal and Nonlinear Dissipative-Soliton Dynamics in Kerr-Microresonator Frequency Combs". *Phys. Rev. Lett.* **121,** 063902 (2018).

114. Lucas, E. *et al.* "Ultralow-noise photonic microwave synthesis using a soliton microcomb-based transfer oscillator". *Nature Communications* **11,** 374 (2020).

115. Levin, Y. "Fluctuation–dissipation theorem for thermo-refractive noise". *Physics Letters A* **372,** 1941–1944 (2008).

116. Merklein, M. *et al.* "Widely tunable, low phase noise microwave source based on a photonic chip". *Opt. Lett.* **41,** 4633–4636 (2016).

117. He, Y. *et al.* "Self-starting bi-chromatic LiNbO3 soliton microcomb". *Optica* **6,** 1138–1144 (2019).

118. Pfeiffer, M. H. P. *et al.* "Octave-spanning dissipative Kerr soliton frequency combs in Si3N4 microresonators". *Optica* **4,** 684–691 (2017).

119. Li, Q. *et al.* "Stably accessing octave-spanning microresonator frequency combs in the soliton regime". *Optica* **4,** 193–203 (2017).

120. Moille, G. *et al.* "Dissipative Kerr Solitons in a III-V Microresonator". *Laser & Photonics Reviews* **14,** 2000022 (2020).

121. Li, J., Lee, H., Yang, K. Y. & Vahala, K. J. "Sideband spectroscopy and dispersion measurement in microcavities". *Opt. Express* **20,** 26337–26344 (2012).

122. Li, J., Diddams, S. & Vahala, K. J. "Pump frequency noise coupling into a microcavity by thermo-optic locking". *Opt. Express* **22,** 14559–14567 (2014).

123. Drake, T. E., Stone, J. R., Briles, T. C. & Papp, S. B. "Thermal decoherence and laser cooling of Kerr microresonator solitons". *Nature Photonics* **14,** 480–485 (2020).

124. Callen, H. B. & Welton, T. A. "Irreversibility and Generalized Noise". *Phys. Rev.* **83,** 34–40 (1951).

125. Lugiato, L. A. & Lefever, R. "Spatial Dissipative Structures in Passive Optical Systems". *Phys. Rev. Lett.* **58,** 2209–2211 (1987).

126. Eggleton, B. J., Poulton, C. G., Rakich, P. T., Steel, M. J. & Bahl, G. "Brillouin integrated photonics". *Nature Photonics* **13,** 664–677 (2019).

127. Kabakova, I. V. *et al.* "Narrow linewidth Brillouin laser based on chalcogenide photonic chip". *Opt. Lett.* **38,** 3208–3211 (2013).

128. Otterstrom, N. T., Behunin, R. O., Kittlaus, E. A., Wang, Z. & Rakich, P. T. "A silicon Brillouin laser". *Science* **360,** 1113–1116 (2018).

129. Ludvigsen, H., Tossavainen, M. & Kaivola, M. "Laser linewidth measurements using self-homodyne detection with short delay". *Optics Communications* **155,** 180–186 (1998).

130. Yuan, Z. *et al.* "Correlated self-heterodyne method for ultra-low-noise laser linewidth measurements". *Opt. Express* **30,** 25147–25161 (2022).

131. Behunin, R. O., Otterstrom, N. T., Rakich, P. T., Gundavarapu, S. & Blumenthal, D. J. "Fundamental noise dynamics in cascaded-order Brillouin lasers". *Phys. Rev. A* **98,** 023832 (2 2018).

132. Do, I. H. *et al.* "Self-stabilized soliton generation in a microresonator through mode-pulled Brillouin lasing". *Opt. Lett.* **46,** 1772–1775 (2021).

133. Bai, Y. *et al.* "Brillouin-Kerr Soliton Frequency Combs in an Optical Microresonator". *Phys. Rev. Lett.* **126,** 063901 (2021).

134. Chauhan, N. *et al.* "Visible light photonic integrated Brillouin laser". *Nature Communications* **12,** 4685 (2021).

135. Bauters, J. F. *et al.* "Ultra-low-loss high-aspect-ratio Si3N4 waveguides". *Opt. Express* **19,** 3163–3174 (2011).

136. Kudelin, I. *et al.* "Photonic chip-based low-noise microwave oscillator". *Nature* (2024).

137. Xue, X. *et al.* "Mode-locked dark pulse Kerr combs in normal-dispersion microresonators". *Nature Photonics* **9,** 594–600 (2015).

138. Wu*, L., Xie*, W., Chen*, H.-J., Colburn, K., Xiang, C., Chang, L., Jin, W., Liu, J.-Y., Yu, Y., Yamamoto, Y., Bowers, J. E., Suh, M.-G. & Vahala, K. J. "AlGaAs soliton microcombs at room temperature". *Opt. Lett.* **48,** 3853–3856. `http://dx.doi.org/10.1364/OL.484552` (2023).

139. Diddams, S. A., Vahala, K. & Udem, T. "Optical frequency combs: Coherently uniting the electromagnetic spectrum". *Science* **369,** eaay3676 (2020).

140. Gaeta, A. L., Lipson, M. & Kippenberg, T. J. "Photonic-chip-based frequency combs". *Nature Photonics* **13,** 158–169 (2019).

141. Zhang, M. *et al.* "Broadband electro-optic frequency comb generation in a lithium niobate microring resonator". *Nature* **568,** 373–377 (2019).

142. Chang, L., Liu, S. & Bowers, J. E. "Integrated optical frequency comb technologies". *Nature Photonics* **16,** 95–108 (2022).

143. Xiang, C. *et al.* "Laser soliton microcombs heterogeneously integrated on silicon". *Science* **373,** 99–103 (2021).

144. Liu, X. *et al.* "Aluminum nitride nanophotonics for beyond-octave soliton microcomb generation and self-referencing". *Nature Communications* **12,** 5428 (2021).

145. Gong, Z., Liu, X., Xu, Y. & Tang, H. X. "Near-octave lithium niobate soliton microcomb". *Optica* **7,** 1275–1278 (2020).

146. Pu, M., Ottaviano, L., Semenova, E. & Yvind, K. "Efficient frequency comb generation in AlGaAs-on-insulator". *Optica* **3,** 823–826 (2016).

147. Steiner, T. J. *et al.* "Ultrabright Entangled-Photon-Pair Generation from an AlGaAs-On-Insulator Microring Resonator". *PRX Quantum* **2,** 010337 (2021).

148. Shu, H. *et al.* "Microcomb-driven silicon photonic systems". *Nature* **605,** 457–463 (2022).

149. Karpov, M. *et al.* "Dynamics of soliton crystals in optical microresonators". *Nature Physics* **15,** 1071–1077 (2019).

150. Carmon, T., Yang, L. & Vahala, K. J. "Dynamical thermal behavior and thermal self-stability of microcavities". *Opt. Express* **12,** 4742–4750 (2004).

151. Cole, D. C., Lamb, E. S., Del'Haye, P., Diddams, S. A. & Papp, S. B. "Soliton crystals in Kerr resonators". *Nature Photonics* **11,** 671–676 (2017).

152. Wang, W. *et al.* "Robust soliton crystals in a thermally controlled microresonator". *Opt. Lett.* **43,** 2002–2005 (2018).

153. Guden, M. & Piprek, J. "Material parameters of quaternary III - V semiconductors for multilayer mirrors at wavelength". *Modelling and Simulation in Materials Science and Engineering* **4,** 349 (1996).

154. Zhang, S. *et al.* "Terahertz wave generation using a soliton microcomb". *Opt. Express* **27,** 35257–35266 (2019).

155. Liu, Y. *et al.* "A photonic integrated circuit–based erbium-doped amplifier". *Science* **376,** 1309–1313 (2022).

156. Markov, I. L. "Limits on fundamental limits to computation". *Nature* **512,** 147–154 (2014).

157. Feldmann, J., Youngblood, N., Wright, C. D., Bhaskaran, H. & Pernice, W. H. P. "All-optical spiking neurosynaptic networks with self-learning capabilities". *Nature* **569,** 208–214 (2019).

158. Yamamoto, Y., Leleu, T., Ganguli, S. & Mabuchi, H. "Coherent Ising machines—Quantum optics and neural network Perspectives". *Appl. Phys. Lett.* **117,** 160501 (2020).

159. McMahon, P. L. *et al.* "A fully programmable 100-spin coherent Ising machine with all-to-all connections". *Science* **354,** 614–617 (2016).

160. Fang, A. W. *et al.* “Electrically pumped hybrid AlGaInAs-silicon evanescent laser”. *Opt. Express* **14,** 9203–9210 (2006).